Pyro-Gel Synthesis:

An Experimental Analysis and Simulation

by

Varun Sagi

A Thesis Presented in Partial Fulfillment
of the Requirements for the Degree
Master of Science

Approved November 2010 by the
Graduate Supervisory Committee:

Taewoo Lee, Chair
Patrick Phelan
Kangping Chen

ARIZONA STATE UNIVERSITY

December 2010

ABSTRACT

Processed pyro-gel contains castor oil with solid component of boehmite (Al-OOH). The pyro-gel is synthesized by heat to convert boehmite to gamma-Al_2O_3 and to a certain extent alpha-Al_2O_3 nano-particles and castor oil into carbon residue. The effect of heat on pyro-gel is analyzed in a series of experiments using two designed and fabricated reactors with the initial temperature as the main factor. The obtained temperature distribution profiles are studied and it is observed that the gel behaves very close to the theoretical prediction under heat. The carbon residue with Al_2O_3 is then processed for twelve hours and then analyzed to obtain the pore distribution of the Al_2O_3 nano-particles and the relation between the pore volume and the pre-heat temperature is analyzed. The obtained pore distribution shows the pore volume of Al_2O_3 nano-particles has direct relation to the pre-heat temperature. The experimental process involving the cylindrical reactor is simulated by using a finite rate chemistry eddy-dissipation model in a non-premixed and a porous mesh. The temperature distribution profile of the processed gel for both the meshes is obtained and a comparison is done with the data obtained in the experimental analysis. The temperature distribution obtained from the simulations show they follow a very similar profile to the temperature distribution obtained from experimental analysis, thus confirming the accuracy of both the models. The variation in numerical values between the experimental and simulation analysis is discussed. A physical model is proposed to determine the pore formation based on the temperature distribution obtained from experimental analysis and simulation.

ACKNOWLEDGMENTS

I would like to thank my advisor Dr. Taewoo Lee for his endless support, encouragement, guidance, and advice without which my research wouldn't have progressed in the right direction. I would also like to thank my committee, Dr. Patrick Phelan and Dr. Kangping Chen for their support.

I would also like to thank Dr. Dong Kyun Seo and Danielle Ladd from the Department of Chemistry for providing me pyro-gel samples and BJH pore distribution analysis without this research wouldn't have taken place. I would also like to thank the Mechanical Engineering department and Arizona State University for giving me this opportunity through their intellectual and financial support.

Lastly, a special thanks to my parents for their continuous support and blessings for the work I choose to pursue.

TABLE OF CONTENTS

Page

CHAPTER Page

LIST OF TABLES

LIST OF FIGURES

Figure Page

Chapter 1

Background and Literature Survey

1.1 Preparation of Pyro-Gel

A gel results from a condensation of molecules or particles in a solvent. It is constituted by tenuous and entangled chains of solid wetted by a liquid which occupies the whole volume located between solid chains. The liquid is a mixture of solvent, unreacted molecules inducing gelation and by-products of chemical reactions. There are many ways to remove the liquid located within the pores of the gel. A dried gel is named “xerogel”. Drying is often performed by a gentle solvent evaporation at temperatures close to room temperature. In the course of solvent evaporation, the shape of the liquid–vapor interface changes with time. The curvature radius of the meniscus decreases (Fig-1) and, associated to this curvature, capillary forces take place. The pressure difference, between vapor and liquid is given by Laplace’s relation

$$\Delta P = - 2\gamma_{LV}/R$$

The liquid is consequently under a tension stress and conversely the solid network is submitted to a compression stress. Because of the weak mechanical properties of the gel network shrinkage occurs. The pore volume of the xerogel is well lower than that of the starting gel. Hence pronounced textural modifications happen. The volume shrinkage of the gel during drying induces an increase of its stiffness.

Figure - 1

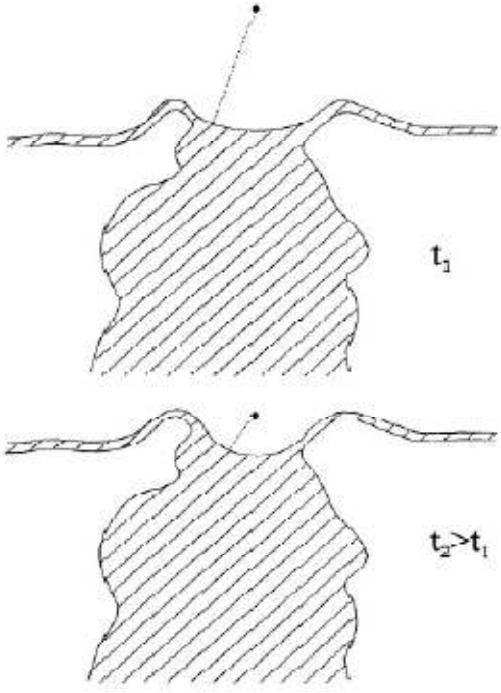

Evolution of the curvature of liquid–vapor meniscus at the surface of a pore as a function of drying time, t (Ref - Sakka and Kozuka, Sol–Gel Science)

At a given time, the solid network is no more compliant and the meniscus recedes in the pores. At this moment, the stress is maximum since the curvature radius corresponds to that of the shrunk pore (assumed cylindrical). Associated to evaporation, the liquid flows from the core of the gel to the surface. This flow is hindered by the solid arms of the gel. A gel is badly permeable because the size of the pores lies mainly within the range 0.2–10 nm indicating that a gel is a mesoporous material. According to the Darcy's law, the liquid flow, J, is related to permeability, D, by the relation

$$J = - D\nabla P/\eta$$

Because of the stress gradient, the solid network may crack. This kinetic approach explains why cracking is related to the evaporation rate. Indeed the evaporation rate controls the liquid flow. A gel dried very slowly will produce a free crack xerogel. Many authors report drying treatments the duration of which is of several months. That is usually done by covering the gels with a plastic film in which many holes are punctured. Cracking of the solid part of the gel is the second drawback usually encountered during drying. Freeze drying and supercritical drying are two processes which are commonly used to circumvent these difficulties. The main reason pyro-gels are different from aero/xero gels is, pyro-gels are prepared by burning rather than drying at the end of the synthesis process.

Solvents used during burning belong to two families: organic and inorganic solvents. The organic solvents are mainly alcohols, ether and acetone. For safety conditions, ether and acetone will be rarely used. Among the alcohols, those having short length are preferred because they do not decompose at high temperature and pressure. Moreover, because of their quite high critical temperature, organic solvents usually react with the solid network. The solvent used in this case is a mixture of tri-glyceride acids called castor oil. An esterification reaction often occurs. In the case of silica gel prepared from hydrolysis of organometallic compounds diluted in alcohol, the nature of the surface of solid particle is modified according to the reaction

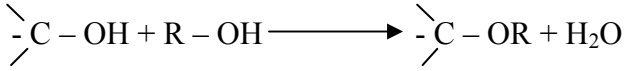

The C–OH surface groups are replaced by chemical groups $-\overset{\diagdown}{\underset{\diagup}{C}} - OR$ which exhibit a hydrophobic effect. A silica aerogel obtained by alcohol SCD floats when placed onto water. With time, air moisture will react again with $-\overset{\diagdown}{\underset{\diagup}{C}} - OR$ Consequently the aerogel becomes hydrophilic according to the reverse reaction

$$-\overset{\diagdown}{\underset{\diagup}{C}} - OR + H_2O \longrightarrow -\overset{\diagdown}{\underset{\diagup}{C}} - OH + R - OH$$

Water absorbs again on the pore walls of the aerogel inducing again capillary forces. The monolithicity of the aerogel can be lost. The second drawback of organic solvent used in supercritical process is associated to the nature of the solid network. Because the required high critical temperature, only gels built up by strong chemical bonds are able to resist the heat treatment. Physical gels are gels formed with quite weak chemical bonds such as hydrogen or Van der Waals. After setting, this sort of gel is easily transformed into a liquid state by a vigorous stirring. These gels are damaged when submitted to a heat treatment. That means that only chemical gels whose the solid network consists of strong (covalent or ionic) bonds are able to be transformed into crack free aerogels. Inorganic gels which obey to these conditions are not very numerous (silica and binary silicates doped with Most of organic gels are not strong enough to be dried using alcohol supercritical drying/burning.

1.2 Constituents of Pyro-Gel

The pyro-gel used in the experimental analysis mainly constitutes of Boehmite (AlOOH) soaked in a wet fuel gel. The wet gel used in this case is castor oil. The main constituents of castor oil is given in the table below

Table – 1

S.No	Acid Name	Average range (%)
1	Ricinoelic acid	85 – 95
2	Oleic acid	2 – 6
3	Linoleic acid	1 – 5
4	Linolenic acid	0.5 – 1
5	Stearic acid	0.5 – 1
6	Palmitic acid	0.5 – 1
7	Dihydroxystearic acid	0.3 – 0.5
8	Others	0.2 – 0.5

Constituents of castor oil

All the acids are in their triglyceride forms.

1.3 Effect of Heat and Oxygen on Pyro-Gel

The pyro-gel when subjected to heat in presence of oxygen undergoes the following reactions

$$4\ AlOOH + O_2 \rightarrow 2\ \gamma\text{-}Al_2O_3 + 2\ H_2O \rightarrow 2\ \alpha\text{-}Al_2O_3 + 2\ H_2O$$

$$C - H \text{ bonds} + \text{limited } O_2 \rightarrow C - C \text{ bonds} + H_2O$$

$$C - H \text{ bonds} + \text{excess } O_2 \rightarrow CO_2 + H_2O$$

The above equations give an insight into the optimum conditions at which the fuel needs to be burned. The boiling point of Al_2O_3 is 313 ^{0}C. If the fuel is burned at an initial temperature close to boiling point, we have what is called as a capillary effect. If Al_2O_3 starts boiling then vapors create capillary suction on the walls of the pores thus compressing them and reducing the pore volume. When the initial temperature of burning is very high (~ 500 ^{0} C) the capillary effect is reduced, retaining the pore size. Burning the fuel in excess oxygen will break the C – H bonds and effect in release of carbon in shape of CO_2. Burning in limited oxygen will break the C – H bonds, but instead of formation and escape of CO_2, C – C bonds are formed, which provide structural support to the pores and prevents it from collapsing.

1.4 Studies of the chemical and pore structures of carbon aero-gels

Carbon aerogels are prepared by the process of synthesizing organic gels from resorcinol and furfural in iso-propanol using HCl as a catalyst and then directly drying in supercritical conditions and carbonizing in nitrogen. This method omits the step of exchanging water with an organic solvent and an organic for carbon dioxide before the supercritical drying. This method is much easier and efficient than the process of synthesizing carbon aerogels by carbon dioxide supercritical drying.

Samples of approximately 0.1 g were heated to 200°C to remove all the adsorbed species. Nitrogen adsorption isotherms were then taken using an ASAP 2000 surface area analyzer. The HK and BJH theories were used for the analysis of the micropore and mesopore distribution, respectively.

The effect of mass density on the pore distribution is observed in the SEM, but doesn't give any quantitative relation. The CA-IPA samples prepared at the same temperature, the micropore volume increases with the decrease in the mass density. The alternative tendency of the micropore volume and the BET surface area of the CA-IPA sample to increase with decrease in mass density is almost the same. The mesopore volume (BJH), single point total pore volume and, the pore diameter, the BJH desorption pore diameter and the average pore diameter have a maximum value with a decrease of its mass density.

Table – 2

Sample No.	CA – 59#	CA – 60#	CA – 57#	CA – 62#	CA – 63#
Gelation Temperature (^{o}C)	60	60	70	70	70
Mass content of reactants (wt %)	11.5	5.9	16.7	11.5	5.9
Mass density of carbon aero-gel (mg/ml)	424	231	479	323	148
BET surface area (m^2/g)	615.3	630.4	557.1	583.5	655.6
Micropore volume (ml/g)	0.186	0.189	0.171	0.177	0.202
BJH desorption cumulative pore volume (ml/g)	1.093	0.810	0.842	0.918	0.744
Single point total pore volume (ml/g)	1.253	0.979	0.981	1.075	0.926
Median pore diameter (nm)	46.2	21.8	30.9	37.4	15.7
BJH desorption average pore diameter (nm)	15.1	11.0	12.2	13.5	10.1
Average pore diameter (nm)	8.15	6.21	7.05	7.37	5.65

Surface area, pore volume and pore diameter of CA-IPA samples

The micropore distribution is analyzed using the HK method. All the CA-IPA samples with various mass densities have a very narrow micropore size distribution and most micropores are concentrated at a diameter of 0.5 nm.

Figure - 2

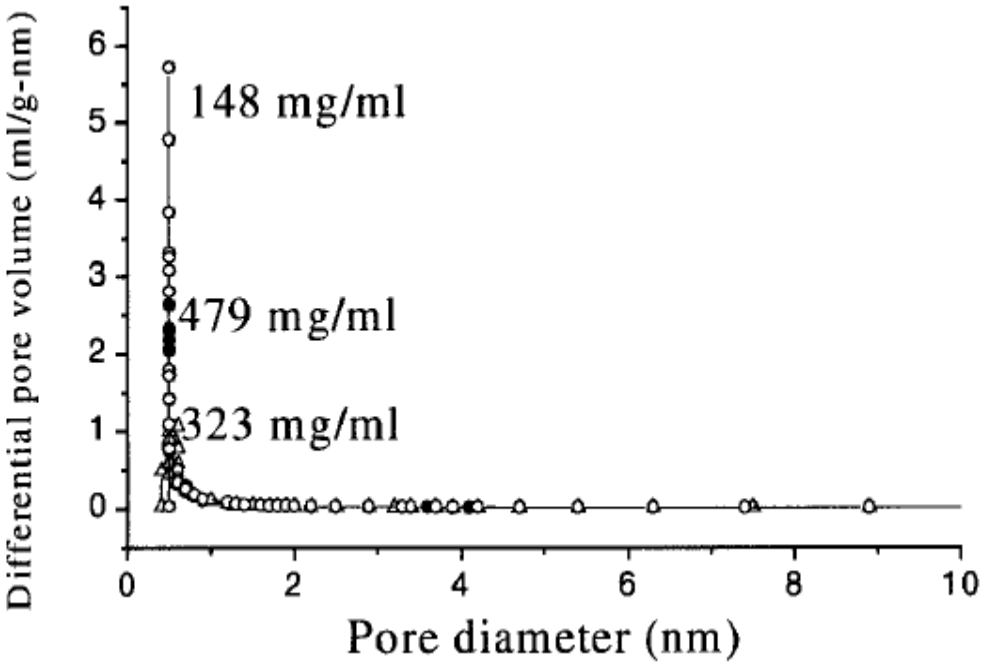

Micropore distribution of CA-IPA samples (Ref - Ruowen Fu, Joe Satcher Jr.)

The mesopore distribution is analyzed using the BJH method. The mesopore size distribution of the CA-IPA samples is widened and the peak value of the distribution is shifted to higher diameters as the mass density decreases.

Figure - 3

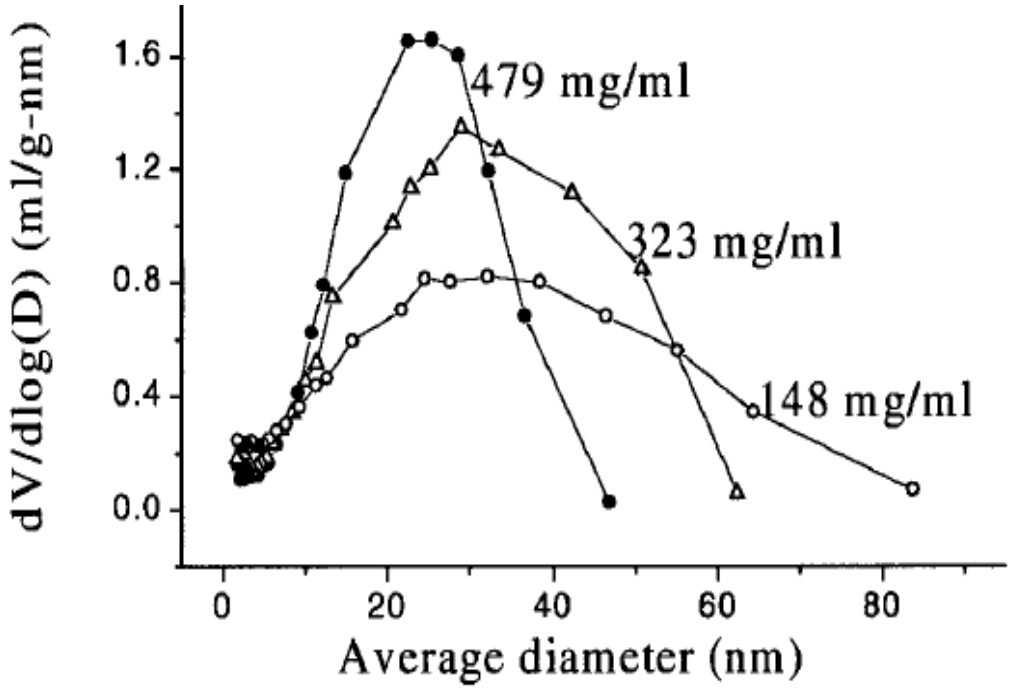

Mesopore distribution of CA-IPA samples (Ref - Ruowen Fu, Joe Satcher Jr.)

The conclusion is the micropore volume of the CA-IPA samples increases with a decrease in mass density whereas the mesopore volume, single point total pore volume, the median pore diameter, the BJH desorption average pore diameter and the average pore diameter have a maximum value at a certain mass density. The micropore size distribution is very narrow and in the range of 0.5 nm diameter and the mesopore distribution is wider with the peaks shifting towards higher diameter as the mass density reduces.

1.5 Synthesis of High Surface Area Alumina Aero-gels

Aluminum Chloride Hexahydrate was first dissolved in pure alcohol ethanol and distilled water. After mixing for an hour at room temperature nitric acid was added for pH adjustment. Propylene oxide as a gelation promoter is added to the mixture. The wet gel was aged for 72 hours and then dried by supercritical carbon dioxide in a supercritical extraction system at 333 K and 24 MPa. The figure below shows the aero-gel preparation of the alumina aero-gels

Figure – 4

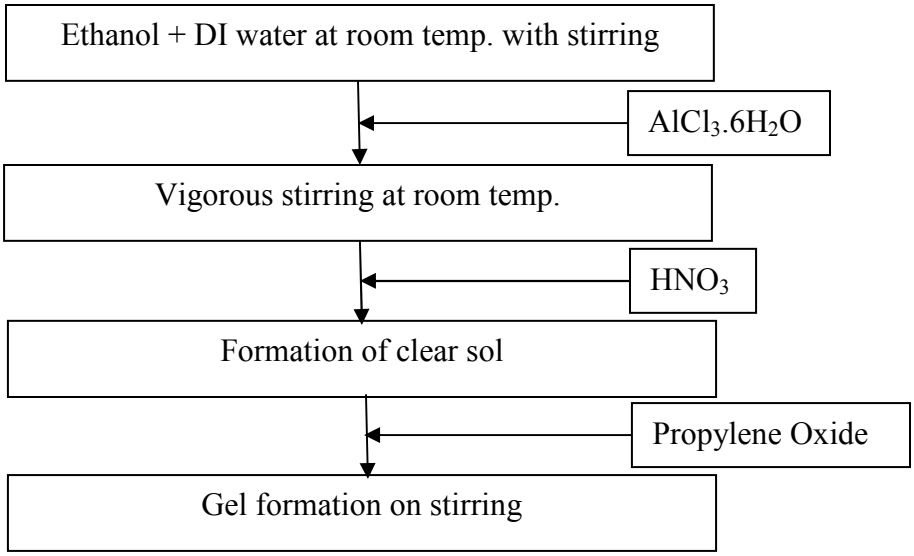

Preparation process of alumina aero-gel

The aero-gel is heated in a tube furnace in flowing helium at 573 K for 2 hours and then in oxygen at 773K for 2 hours. BET surface areas, pore volumes and pore distributions are measured by nitrogen adsorption-desorption at 77K using a Micrometrics ASAP 2000. The mesopore size distributions were calculated applying the BJH method t the deposition branch of the isotherm. Prior to measurement all samples were outgases at 383 K.

Textural properties of alumina aerogel and xerogel before and after the heat treatment process are shown in the table below.

Table – 3

Heat treatment (K)	Alumina Aerogel			Alumina Xerogel		
	S_{BET}	V_P	D_P	S_{BET}	V_P	D_P
383 – vacuum – overnight	795	4.2	21.6	325	0.31	3.8
573 – He – 2 hrs	755	4.1	21.8	416	0.41	4.0
773 – O_2 – 2 hrs	723	3.5	22.4	359	0.48	5.4
1073 – O_2 – 2 hrs	514	2.9	22.7	211	0.43	8.2
1173 – O_2 – 2 hrs	390	2.2	22.8	169	0.39	9.2
1273 – O_2 – 2 hrs	247	0.2	19.1	119	0.32	10.8

Surface area, pore volume and pore diameter (Ref - Minh Nguyen, Tae Park)

Where S_{BET} is BET surface area (m^2/g), V_P is total pore volume (cc/g) and D_P is the average pore diameter (nm).

In general, aerogel samples after calcination at 773 K have a surface area above 700 m^2/g, which is greater than any commercially available sample and alumina aerogel prepared by fast sol-gel synthetic route using alkoxide. All aerogel samples treated at different temperatures exhibit mesoporosity in the range of 19-23 nm and the corresponding pore size distribution curves become smaller. The pore volume and average pore diameter of the xerogel sample are significantly smaller than those of the aerogel samples. However, both aerogel and xerogel samples maintained relatively high surface area of 200 m^2/g and 100 m^2/g, respectively even after additional treatment at 1273 K.

The different textural characteristics between aerogel and xerogel samples are most likely due to the different processing conditions each was subjected to. The evaporation of the ethanol from the xerogel sample exerted substantial capillary forces on the gel's pore structure, which resulted in shrinkage of the pores, relative to the aerogel sample. Additional heat treatment up to 1273 K did not radically change the textural characteristics of the calcined alumina aerogel. These results suggest that our alumina aerogel has the inherently rigid porous network structure of the polymeric gels. In the case of the xerogel, the increase of the surface area and pore volume, after calcinations at 723 K, was a result of the removal of organic residues from micro-mesopores, rendering the surface accessible for the physical adsorption of nitrogen at 77 K. However, the surface area and pore volume of the calcined xerogel decreased after heat treatment at 773 K. This is probably due to the exothermic phase transformation process evidenced by X-ray diffraction (XRD) and thermal analysis.

1.6 Thermal Evolution of Alumina prepared by the Sol-Gel technique

Metastable forms of aluminium oxide called ' 'transition aluminas" are used as adsorbents, supports of catalysts, coatings, and soft abrasives. They are usually prepared by thermal treatment or hydrothermal transformations of aluminium hydroxides and by oxidation of aluminium. In particular, boehmite (A1OOH) transforms to different transition aluminas, finally giving rise to the thermodynamically stable phase: α-alumina (corundum). The origin and the granulometry of the starting boehmite, the presence of impurities, the thermal history, and the thermal treatment conditions (time and temperature) notably affect the temperature of each transformation. According to several authors, the approximate temperatures of these transformations in the sequence of crystallization are boehmite to y (300°C), 7 to 6 (850°C), 6 to σ (1100°C), and σ to α (> 1200°C).

The studied material was prepared by the sol-gel procedure by hydrolyzing aluminium isopropoxide (AIP) at room temperature in an excess of bidistilled water (100 mol of water per mol of alkoxide), under vigorous stirring. AIP was prepared by reacting aluminium with boiling isopropanol, using $HgCl_2$ as the catalyst. The peptization of the sol was performed at 90°C using aluminium nitrate as the peptizing agent, with a molar relation of $A1(NO_3)_3$/AIP of 0.07/1. The gel was dried at 80°C, ground in agate mortar, and sieved through 400 mesh (37 /m). Differential (DTA) and gravimetric (TGA) thermal analyses were done for the dried gel at the heating rate of 10°C/min, under an air atmosphere. The samples were treated at increasing temperatures between 300 and 1200°C in a Pt

crucible inside an electrical furnace under an air atmosphere. The heating rate was 10°C/min up to the desired temperature. Samples were maintained for 1 h at this temperature and rapidly cooled outside the furnace. Specific area measurements were made according to the BET method using a single-point technique in a Monosorb Quantachrome machine. Samples were previously subjected to an outgas treatment at 100°C during 120 min in a 70% N_2/30% He flow.

Figure - 5

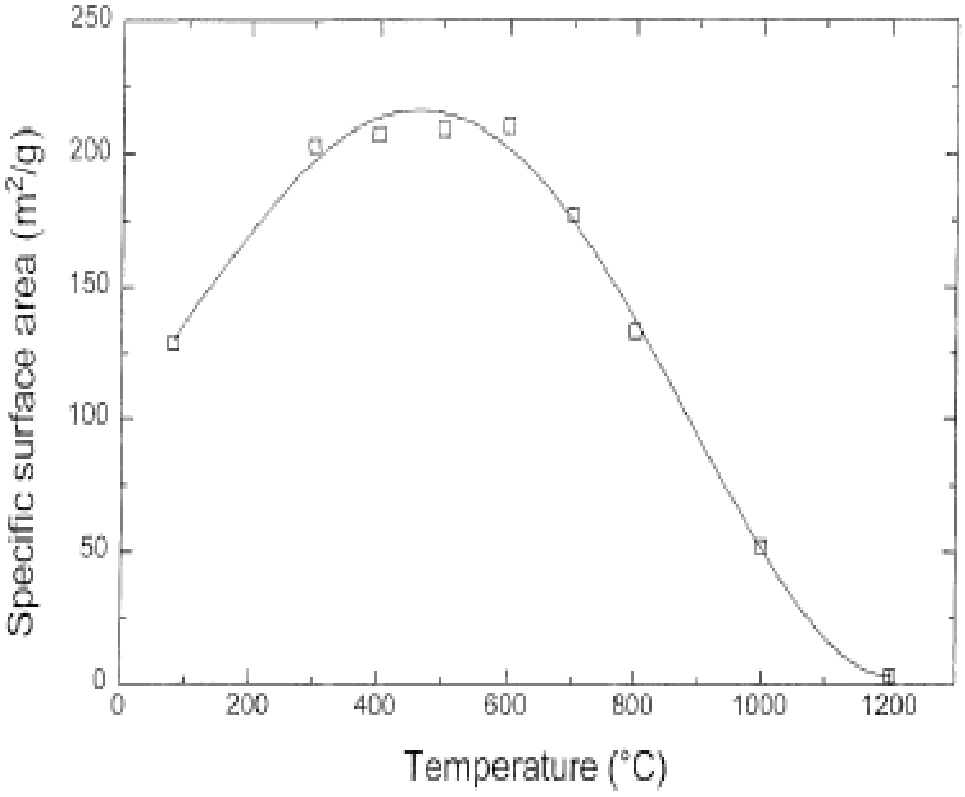

BET surface area (Ref - G. Urretavizcaya, J Sanz)

The figure above shows the specific surface area (BET) values as a function of temperature. The initial increment of the specific surface area from 130 to 200

m2/g in the range of 100-300°C could be attributed to the elimination of organics and adsorbed water produced before the formation of boehmite. During the transformation of this phase into 7-Al_2O no variation of the specific surface area is detected; however, a progressive diminution is observed during the transformation. The sample treated at 1200°C shows a BET area of 3.4 m^2/g, a typical value for nonporous materials.

When alumina obtained by the sol-gel procedure is heated at 300°C, boehmite formation is accompanied by an increase in the specific surface area. γ-Alumina is formed after thermal treatment of boehmite at 400°C, without a change in the specific surface area. Al occupies not only octahedral sites as in the boehmite phase but also tetrahedral ones. The γ-$A1_2O_3$ phase obtained between 600 and 800°C exhibits an important vacancy ordering over tetrahedral structural sites, which progresses in samples heated at 800 °C (5-alumina formation). The distribution of cations changes between 800 and 1000°C, by a progressive decrease in the amount of tetrahedral Al. At 1000°C, the 0-alumina phase is formed and a-alumina is also detected. Finally, at 1200°C α-alumina is the only phase present. Its formation leads to the complete elimination of tetrahedral aluminium and an important diminution of the specific surface area.

1.7 Synthesis and pore analysis of aerogel-glass fiber composites by ambient drying method

Flexible aerogel–glass fiber composites were prepared by varying colloidal silica and tetraethylorthosilicate (TEOS)-based sol fractions. After immersing glass fiber matrices into silica sol with different volume fraction of colloidal silica sol, it was surface-modified into trimethylchlorosilane/n-hexane solution and heat-treated at 230°C in ambient atmosphere. From the results of Brunauer–Emmett–Teller (BET) surface area, Barrett–Joyner–Halenda (BJH) pore size analyses, apparent density and porosity studies, it was thought that microstructures of aerogel composites like pore size and specific surface area were greatly affected by precursor sol. Aerogel composites made of only colloidal silica showed greater density and lesser porosity, smaller pore size and specific surface area than those of aerogel composites synthesized from colloidal and TEOS-based mixed sols.

Silica aerogels could be synthesized from various starting materials like sodium silicate and silicon alkoxide such as tetraethylorthosilicate and tetraethylorthosilicate. Kistler firstly synthesized silica aerogels using sodium silicate, but afterwards Teichner group invented another synthetic method using TMOS, which could decrease the time of aerogel synthesis by omitting solvent exchanging process. Supercritical drying method is normally used to transform gel to aerogel in autoclave, which remove solvent without cracking at a critical temperature and pressure (T_c = 31°C, P_c = 939 psi for CO_2). Ambient pressure drying method to prepare aerogel without using supercritical drying was

developed, which surface-modified silica gel by silylation to annihilate the capillary liquid tension. In this study, silica aerogel composites were prepared by immersing glass fiber matrix into silica sol, gelled afterward and surface-modified in trimethylchlorosilane (TMCS) solution. The pore structures of aerogel composites were investigated by changing volume ratio of colloidal silica-based sol and tetraethylorthosilicate-based sol.

Sodium silicate which contains 10% Na_2O and 30% SiO_2 was ion-exchanged by flowing through Amberlite resin to remove sodium ion. The colloidal silica sol was diluted to 12 wt% silica contents and ethanol was added to get 6 wt% silica-contained sol. The silica sol synthesized from sodium silicate sol is called colloidal silica-based sol afterward. Tetraethyl orthosilicate-based sol was synthesized by adding TEOS to ethanol and HNO_3 was added as a catalyst. The molar concentration of TEOS was 1 M, equivalent to 6 wt% silica contents. The volume ratio of colloidal silica sol and TEOS-based silica sol was changed from 0 to 100%. WT-100 sample contained 100% colloidal silica sol and WT-0 was comprised of 100% TEOS-based sol with no colloidal silica sol. The volume percentage of colloidal silica-based sol in total silica sol was 0 for WT-0, 25 for WT-25, 50 for WT-50, 75 for WT-75, and 100% for WT100. Glass fiber matrix was immersed in silica sol and aged in ethanol for 2 days. After ageing, the gelated glass fiber matrix was solvent exchanged and surface-modified, simultaneously, in 6 vol% of ispropylalcohol and TMCS and normal hexane solution by immersing it for 2 days. The molar concentration of TMCS was fixed at 0.2:1 for pore solvent within silica gel. The surface modified gelled glass fiber

composite was dried at room temperature for 24 h and 50 °C for 4 h. It was heat-treated at 230 °C for 2 h of which ramp rate was 1 °C/min. Specific surface area and pore size distribution of aerogel composites were analyzed by BET and BJH nitrogen gas absorption and desorption method. The apparent density and porosity of aerogel composites were analyzed by Archimedes principle.

Pore volume and pore size were analyzed by BJH method. Nitrogen adsorption and desorption method can be applied to pores of which sizes are in the rage of 17–3000 Å. Fig. below shows the variations of pore volume and pore size of aerogel composites with colloidal silica sol contents. WT-100 aerogel composites had 1.5 cm^3/g pore volume, WT-75 and WT-50 had 2 cm^3/g and it was increased to 4 cm^3/g for WT-25 and decreased again to 2.4 cm^3/g for WT-0. Pore size variations with colloidal silica sol contents showed almost the same trends as the pore volume variations. The pore size of WT-100 was 90 Å, 150 Å for WT- 75, and 135 Å for WT-50. It increased to 265 Å for WT-25 and decreased to 210 Å for WT-0.

Figure - 6

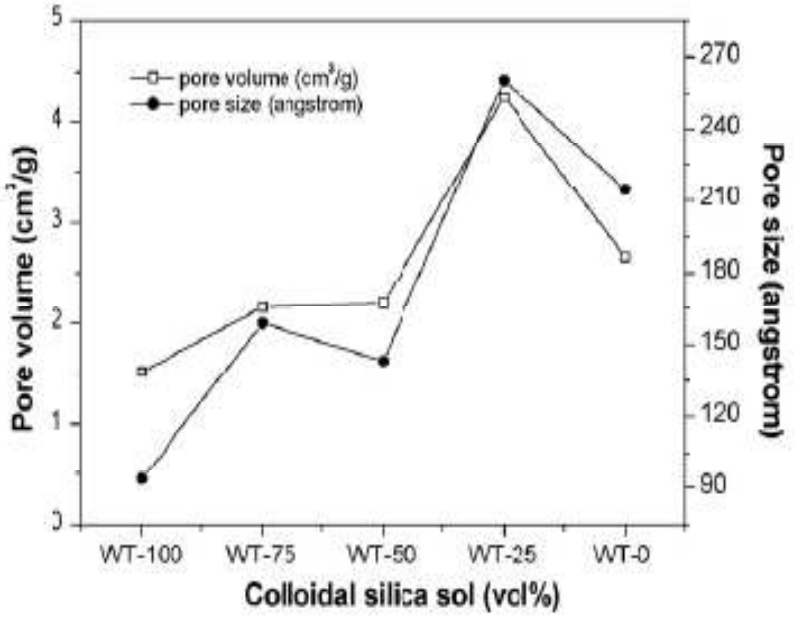

Pore volume Vs colloidal volume (Ref - Chang-Yeoul Kim, Jong-Kyu Lee)

Specific surface area changes with colloidal silica contents measured by BET method are shown in Fig. below. It increased from 380 cm^2/g for WT-100 to 455 cm^2/g for WT-50, and decreased to 380 cm^2/g for WT-0. This result showed that specific surface area and pore volume were affected by using different precursors for the synthesis of aerogel composites. For WT-100, springback effects after surface modification was not enough to restore its volume from contracted state of gel. On the contrary, WT-0 made of only TEOS-based silica sol showed the smaller pore sizes, pore volume and specific surface area than those of colloidal silica and TEOS-based mixed silica aerogel composites. It indicates that WT-0 is comprised of homogeneous small size of pores, which is confirmed by analysis of pore size.

Figure - 7

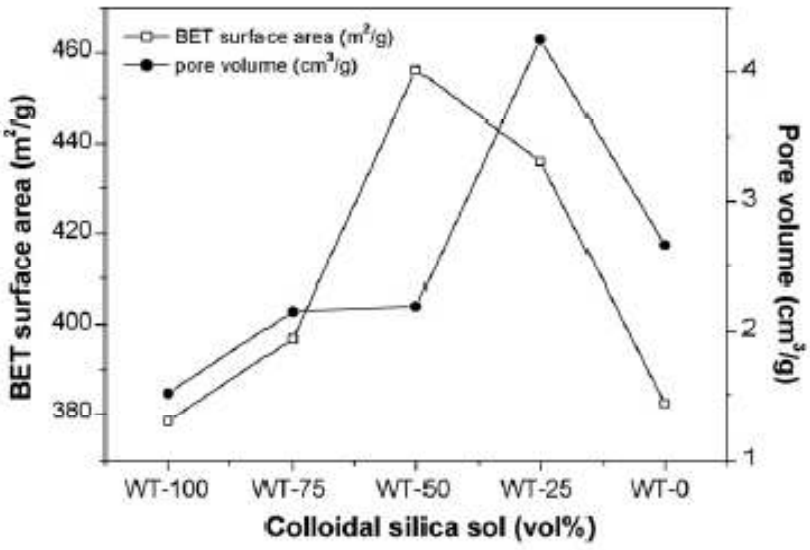

BET surface area Vs colloidal volume (Ref - Chang-Yeoul Kim, Jong-Kyu Lee)

Fig, below shows pore size distributions of aerogel composites. It is known that aerogel composites contained mesopores (20–500 Å pores) and macro pores (above 500 Å) from pore size distribution graphs. Most pores of WT-100 are known to be mesopores below 500 Å and its peak of smallest pore was 63 Å. WT-0 aerogel composite was comprised of 190 Å pores and 2400 Å pores. WT-25 samples had three main pores, 146 Å, 507 Å, and 1600 Å. It is known that aerogels are mainly comprised of mesopores below 500 Å. Considering the upper limit pore size is 3000 Å by nitrogen absorption and desorption method, silica aerogel composite could have macropores larger than 3000 Å . The fact is supported by smaller pore volume than expected; for example, in the case of 0.12 g/cm^3 aerogel composites with 90% porosity, it should have 7.5 cm^3/g of pore volume. The fact

indicates that silica aerogel/glass fiber composites had also macropores above 3000 Å.

Figure - 8

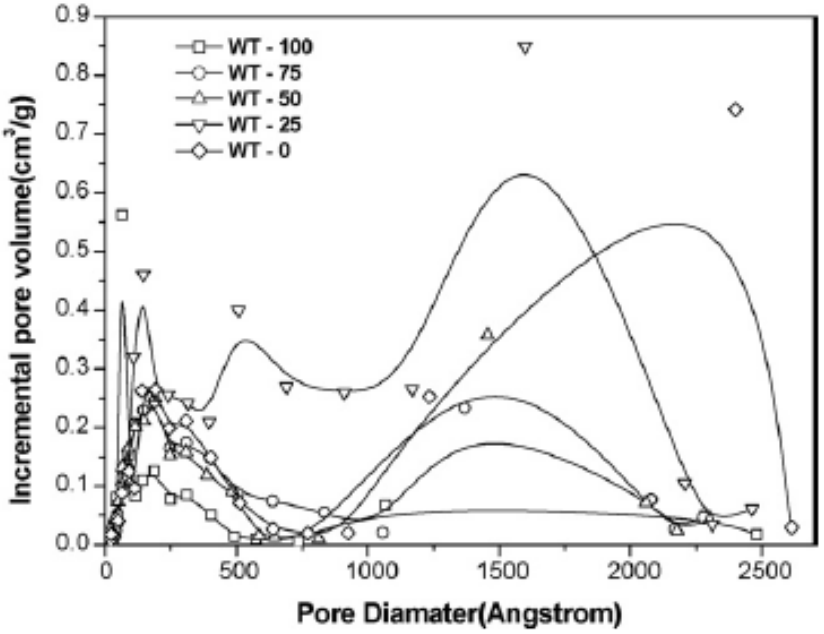

Pore distribution of WT samples (Ref - Chang-Yeoul Kim, Jong-Kyu Lee)

Fig. below shows the apparent pore volume measured by Archimedes principle and pore volume variations investigated by BJH method.

Figure - 9

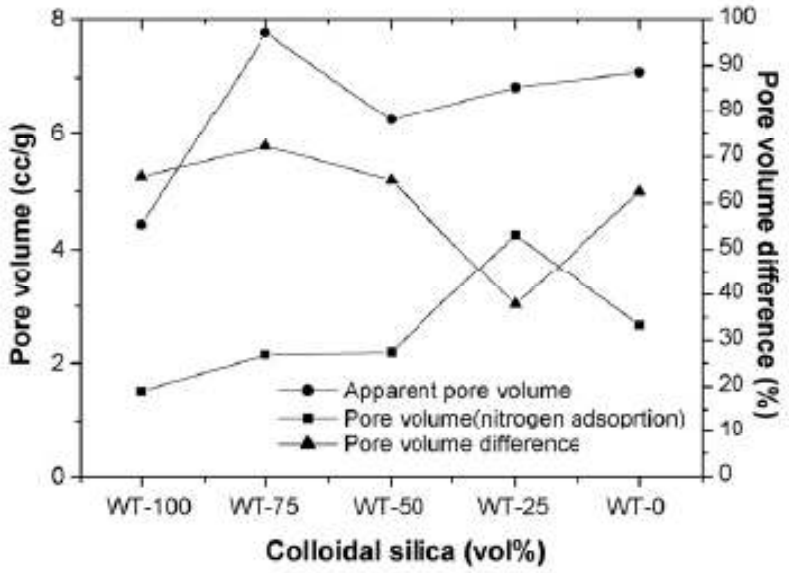

Pore volume Vs colloidal volume (Ref - Chang-Yeoul Kim, Jong-Kyu Lee)

As summarized in the table below, WT-0 has 1.52 cm^3/g pore volume (BJH) and 4.43 cm^3/g apparent pore volume, of which difference was 65.7%. WT-0 had the smallest apparent pore volume and pore size. WT-75 had the largest apparent pore volume, 7.77 cm^3/g, but had only 2.15 cm^3/g pore volume (BJH). It means thatWT-75was comprised of about 70% macropores above composites. It means that WT-75 was comprised of about 70% macropores above 3000 Å. WT-50 had 6.25 cm^3/g for its apparent pore volume and 2.19 cm^3/g for its pore volume (BJH), which tells that WT-50 had 65% macropore portions. WT-25 had its apparent pore volume 6.83cm^3/g and pore volume (BJH), 4.25cm^3/g. The

macropore percentage above 3000 Å was the smallest, 38% for WT-25. For WT-0, apparent pore volume was 7.09cm^3/g and pore volume (BJH) was 2.66cm^3/g and its difference was 62.5%. The reason why WT-25 had the largest pore volume (BJH) and WT-0 had a decreased pore volume (BJH) was not clear at the present state. It is inferred that aerogel composites are comprised of mesopores and macropores over the limit of measurement range of nitrogen gas adsorption and desorption method. Pore size and volume are influenced by colloidal silica sol and alkoxided-based silica sol ratio.

Table – 4

Sample	Apparent Density (g/ml)	Porosity (%)	Apparent pore volume (ml/g)	BJH Pore volume (ml/g)	Pore size (Å)	Surface area (m^2/g)
WT - 100	0.195	86.3	4.43	1.52	94	378
WT – 75	0.116	90.1	7.77	2.15	159	397
WT – 50	0.143	89.4	6.25	2.19	143	456
WT – 25	0.133	90.8	6.83	4.25	260	436
WT – 0	0.127	90.0	7.09	2.66	215	382

Properties of silica aero-gel composites (Ref - Chang-Yeoul Kim, Jong-Kyu Lee)

Flexible silica aerogel composites were synthesized by compositing glass fiber and silica aerogel from different volume ratio of colloidal silica sol and TEOS-based sol. Surface modification in TMCS solution in n-Hexane and heat-treatment at 230°C made it possible for silica–aerogel composites to dry at ambient pressure. Aerogel composites from mixed silica sols of colloidal silica and TEOS-based silica sols showed smaller density, higher porosity, and greater surface area.

1.8 High surface area carbon aerogel Monoliths with hierarchical porosity

Synthesis and structural characterization of monolithic carbon aerogel (CA) materials that possess both high surface areas and hierarchical porosity is described in the following. Thermal activation of a macroporous CA structure, one that was derived from an acetic acid-catalyzed sol–gel polymerization reaction, yields monolithic materials with large pore volumes and surface areas exceeding 3000 m^2/g. Given the flexibility of CA synthesis, this approach offers viability to engineer new materials for use as catalyst supports, electrodes, capacitors and sorbent systems.

The design of new porous carbon materials holds technological promise for a variety of applications, including catalysis, adsorption and energy storage. The utility of these materials is derived from their high surface areas, electrically conductive frameworks and chemical stability. One area of carbon research that has received significant attention is the use of these porous materials as sorbents for hydrogen. Safe and efficient storage of hydrogen is considered one of the main challenges associated with utilization of this fuel source in the transportation sector. We recently reported on the hydrogen sorption properties of high surface area carbons that were prepared from carbon aerogels (CAs). Carbon aerogels are unique porous solids with network structures consisting of interconnected carbon particles and, as a result, these materials exhibit many interesting properties, such as high surface-to-volume ratios, continuous porosities and high electrical conductivity. In the course of that work, we developed a synthetic approach to fabricate CAs with BET surface areas over 3000 m^2/g. These surface area values

are the highest that we are aware of for CAs and are comparable to those of the highest surface area activated carbons. In the work presented here, we describe our approach to the design of these high surface area carbons. Our synthetic strategy involves the thermal activation of a CA material with structural features (particles and pores) on the micrometer scale. This approach not only provides access to high surface areas in CA materials, but also affords monolithic materials with bimodal porosity (macro- and micropores). Hierarchically porous carbons of this type present a number of advantages over unimodal carbon structures in terms of diffusion efficiency and surface area, and thus these materials should also have utility as new catalyst supports or electrodes for electrochemical devices.

Thermal activation of CAs involves the controlled burn-off of carbon from the network structure in an oxidizing atmosphere, such as carbon dioxide, resulting in the creation of new micropores as well as opening of closed porosity in the CA framework. Therefore, access to high surface areas in activated CAs requires careful design of the pre-activated carbon framework, as the morphology of the particles that comprise the network structure will ultimately determine the textural properties of the activated material. The microstructure of traditional CAs, consisting of nanometer-sized carbon particles and tortuous pore structures, can both limit the surface areas attainable through activation and lead to inhomogeneous burn-off in monolithic samples. By utilizing CAs with larger pore and particle sizes, however, these issues can be mitigated and monolithic carbons with high surface areas and bimodal pore structures can be readily attained. The synthesis of pre-activated CA structures with larger features can be

performed in a number of ways. Carbon aerogels are typically prepared through the sol–gel polymerization of resorcinol with formaldehyde in aqueous solution to produce organic gels that are then supercritically dried and subsequently pyrolyzed in an inert atmosphere. The amount and type of catalyst used in the polymerization reaction dictates the size, shape and connectivity of the primary network particles and, therefore, can be used to influence the structural properties of the resultant CA. One method to generate CAs with larger structural features is the use of low catalyst concentrations in the polymerization reaction. Alternatively, the use of acid catalysts in the sol–gel reaction has also been shown to generate porous structures with network and pore features on the micrometer scale. For the preparation of the CAs used in this study, acetic acid was selected as the reaction catalyst since the process not only affords macroporous carbon structures, but the monolithic products exhibit enhanced mechanical integrity relative to traditional CAs.

For the synthesis of the pre-activated CA, resorcinol (12.3 g, 0.112 mol) and 37% formaldehyde solution (17.9 g, 0.224 mol) were dissolved in water (15 ml), followed by the addition of glacial acetic acid (0.44 g, 0.007 mol). The reaction mixture was then transferred to glass molds and cured at 80 °C for 72 h. The resultant organic hydrogels were washed with acetone to remove the water and then dried with supercritical CO_2. The organic aerogels were subsequently carbonized at 1050 °C for 3 h under an N_2 atmosphere, yielding CA monoliths with densities 0.55 g/cm^3. The activation of these materials was carried out under flowing CO_2 (10 sccm) at 950 °C. The activated CAs are designated as ACA-x,

where x is the activation time in hours. Microstructural characterization was performed using scanning electron microscopy (JEOL 7401-F). Textural properties were determined using N_2 adsorption–desorption techniques (ASAP 2010 Surface Area Analyzer, Micromeritics). Surface areas and pore volumes were determined using Brunauer–Emmett–Teller (BET) and Barrett–Joyner–Halenda (BJH) methods, respectively, while micropore volumes were calculated from t-plot analysis.

Table - 5

S.No	Sample	Burn-off (%)	BET surface area (m^2/g)	Total pore volume (cm^3/g)	Micropore pore volume (cm^3/g)
1	CA	-	463	0.195	0.193
2	ACA-2	43	1496	0.75	0.559
3	ACA-3	60	2276	0.93	0.583
4	ACA-4	71	2450	1.05	0.423
5	ACA-5	75	2803	1.21	0.273
6	ACA-6	85	3125	1.88	0.014

Textural properties of inactivated and activated CAs

To determine the effect of activation on the textural properties of this CA structure, cylindrical monoliths of the material were exposed to a stream of CO_2 at 950 °C for different soak times. Examination of the activated structures by SEM showed smaller network ligaments relative to the inactivated material. Each of the activated samples exhibited typical type II nitrogen adsorption–desorption

isotherms. As the activation time is increased, the isotherms for the ACAs show increased adsorption at low relative pressures, indicating the formation of new porosity within the CA monoliths. At shorter activation times, this new porosity is in the form of micropores, as evidenced by the increased micropore volume measured for ACA-2 and ACA-3. At longer activation times, however, these micropores are widened to sizes that cross the micropore–mesopore boundary. The development of supermicropores and/or small mesopores is confirmed not only by the diminished micropore volume at longer treatment times but also the slight hysteresis in the isotherm for ACA-6. Nevertheless, the BET surface areas and total pore volumes of the activated materials continue to increase with increasing activation times. While this general trend is similar to those observed in other activated CA systems, the key difference here is that the micrometer-sized network morphology of the pre-activated CA allows access to surface areas in the ACAs in excess of 3000 m^2/g. Interestingly, all of the activated materials remained monolithic despite the significant mass loss during thermal treatment. As stated above, this observation is important as the ability to readily fabricate porous carbons as monoliths can be applied to the design of new catalyst supports or electrodes for electrochemical devices.

1.9 Determination of pore volume and area distributions in porous substances

A technique for estimating the volume and area of porous adsorbents available to molecules of various sizes is described in the following. This technique was developed to deal with relatively coarsely porous adsorbents exhibiting a wide range of pore sizes, but the procedure to be described appears to be applicable to porous solids of any nature.

Wheeler proposed a theory which is a composite of BET multilayer adsorption and capillary condensation viewpoints. This theory can be summarized by the equation

$$V_s - V = \prod \int_{r_{p_n}}^{\infty} (r - t)^2 L(r) dr$$

where Vs is the volume of gas adsorbed at saturation pressure, V is the volume of gas adsorbed at pressure p**,** L(r)dr is the total length of pores whose radii fall between r and r + dr. r_{p_n} is the critical radius, that is, the radius of the largest pore still completely filled with liquid adsorbate at any particular pressure and t is the multilayer thickness which is normally built up at pressure p. Wheeler considered the radius of the pore to be equal to the sum of the multilayer thickness as calculated from the BET theory and the radius normally calculated from the simple Kelvin equation. He also suggested that the pore size distribution, L(r), may be approximated by a simple Maxwellian or Gaussian distribution.

Shull pointed out that the BET thicknesses become much larger than experimental thicknesses for flat surfaces in the high pressure region. Shull

proposes the use of experimental data taken-from nitrogen isotherms for crystalline materials, for the determination of the multilayer thickness, t, in the Wheeler theory. He then developed a simplified method for fitting the experimental data to Maxwellian or Gaussian distribution functions.

Almost simultaneously Oulton proposed a method for determining the pore distribution from the isotherm without the necessity of assuming a definite form for the distribution. He corrects for physical adsorption on the walls of pores empty of capillary condensed adsorbate, hereafter termed capillary condensate by assuming that the thickness of the physically adsorbed layer is constant and equal to that of the statistical number of monolayers at the relative pressure of the hysteresis point.

This following will show that the assumption of a simple Gaussian or Maxwellian distribution of pore sizes is inadequate for many adsorbents. It will also show that Oulton's assumption of constant thickness for the physically adsorbed layer, while adequate for a finely porous material such as that to which he applied it (a cracking catalyst with a pore area maximum at radius 26.5 Å**.),** is inadequate to deal with more coarsely porous adsorbents. A formal analysis of the relationship between nitrogen desorption isotherms at liquid nitrogen temperatures and the distribution of pore volume and area with respect to pore radius will be made on the assumption that equilibrium between the gas phase and the adsorbed phase during desorption is determined by two mechanisms:

(1) physical adsorption on the pore walls (which would occur

to the same extent whether the area involved constituted walls of pores or a flat surface impenetrable to nitrogen), and

(2) capillary condensation in what Oulton has called the "inner capillary volume."

Results of the analysis will be applied to several adsorbents utilizing the experimental data used by Shull to provide a functional relationship between thickness of physically adsorbed layer and relative pressure, and utilizing the classical Kelvin equation, relating vapor pressure depression to capillary radius, to define the relationship between volume of capillary condensate and relative pressure.

Consider a system of open ended, cylindrical pores (Fig. 10) such that all pores of equal radius can be regarded as responding in the same way with respect to changes of relative pressure of the adsorbate. Assume that the relative pressure P/P_0 differs infinitesimally from unity so that substantially all pores are filled with liquid. The largest pores have a radius r_{pl}. Upon its surface is a physically adsorbed layer of molecules of statistical thickness t_l. Within this physically adsorbed layer is the inner capillary with radius r_k, from which evaporation occurs as P/P_o is lowered.

Under the equilibrium conditions specified, the relationship between the pore volume, V_{pl} and the inner capillary volume, V_{kl} is

$$V_{pl} = V_{kl} \quad r_{pl}^2/r_{kl}^2$$

However, this relationship is not useful since V_{kl}, is unknown.

Figure – 10

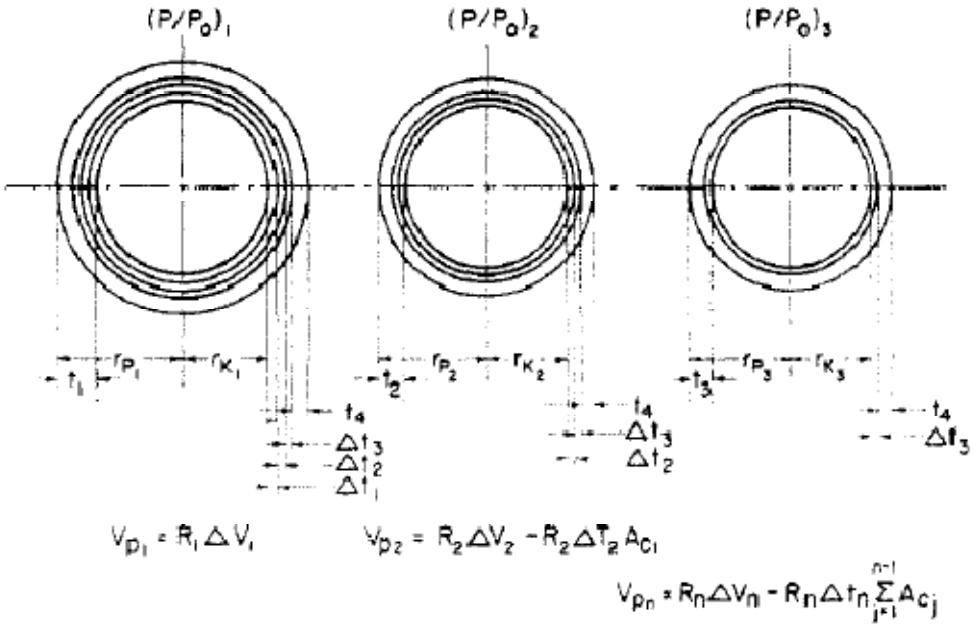

Schematic representation of desorption mechanism (Ref – Elliot P. Barrett, Leslie G. Joyner and Paul P. Halenda)

To obtain useful data, it is necessary to lower $(P/P_o)_1$ to a smaller value $(P/P_o)_2$. This will result in the desorption of a measurable volume of adsorbed gas, ΔV_1. The reduction in relative pressure will result not only in emptying the largest pore of its capillary condensate, but also in a reduction in thickness of the physically adsorbed layer by the amount Δt_l. As a consequence of the reduction in relative pressure and the attendant desorption, may be rewritten as

$$V_{p1} = R_1 \Delta V_1$$

where $R_1 = r_{pl}^2/(r_{k1} + \Delta V_1)^2$ and ΔV_1 is the observed volume of gas desorbed.

A complication enters when one attempts to apply similar reasoning to the obtaining of the volume of the second pore by lowering $(P/P_0)_2$ to $(P/P_0)_3$. When this is done, the volume of liquid desorbed is not only that which comes from the

second pore but also includes that from a second thinning of the physically adsorbed layer left behind in the first pore. If the volume which is released by this thinning is designated as $V_{\Delta t_2}$ then

$$V_{p2} = R_2 (\Delta V_2 - V_{\Delta t_2})$$

Where $R_2 = r_{p2}^2/(r_{k2} + \Delta V_2)^2$

Inspection of Fig. 10 shows that

$$V_{\Delta t_2} = \prod L_1(r_{k1} + \Delta t_1 + \Delta t_2)^2 - \prod L_1(r_{k1} + \Delta t_1)^2$$

Where L_1 is the length of the pore.

Although it would not be too laborious to evaluate $V_{\Delta t_2}$ where the thinning occurs from the walls of only one pore, it is obvious that as a greater number of pores become involved such a calculation would soon become impractical.

An alternate expression for $V_{\Delta t_2}$ is given below,

$$V_{\Delta t_2} = \Delta t_2 \, Ac_1$$

Where Ac_1 is the average area from which the physically adsorbed gas is desorbed. The above equation can be generalized to represent any step in the step-wise desorption by writing in the form

$$V_{\Delta t_n} = \Delta t_n \sum_{j=1}^{n-1} Ac_j$$

The above equation is the sum of the average area in unfilled pores down to, but not including, the pore that was emptied of capillary condensate in the nth desorption. By proper substitutions the generalized equation for V_{pn} is

$$V_{pn} = Rn \, \Delta Vn - \Delta t_n \sum_{j=1}^{n-1} Ac_j$$

The above equation is still unsatisfactory as a computing device because the quantity Ac for any one size of empty pore is not a constant but varies stepwise with each successive decrease in P/P_0. On the other hand A_p, the area of each pore, is a constant which can be calculated from its volume by the relationship $A_p = 2Vp/r_p$ and the successively computed A_p's can be cumulatively summed so that at any step in the desorption ΣA_p is a known quantity. Therefore, if some facile means for computing ΣAc from ΣA_p can be found, above equation will become a practical device for computation. The procedure which has been devised for obtaining a practicable means for computing ΣAc from ΣA_P is exemplified by Fig. 11.

Figure - 11

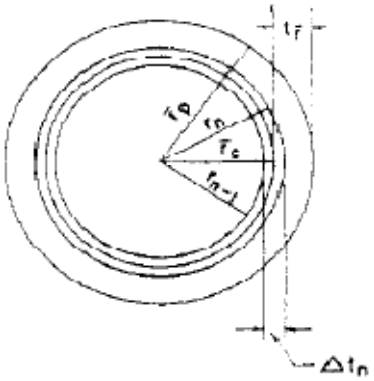

$$V_{\Delta t} = A_c \times \Delta t$$

$$A_c = A_p \times \frac{\bar{r}_p - t\bar{f}}{\bar{r}_p} = A_p \times c$$

Relation of $V\Delta t$ to r_p at n^{th} step (Ref – Elliot P. Barrett, Leslie G. Joyner and Paul P. Halenda)

It is assumed that all capillaries emptied a relative pressure decrement have an average radius, r_p, between the radii corresponding to the upper and lower values adsorbed layer of a previously emptied pore of radius r_p during the n^{th} desorption

step. The capillary radius before desorption is r_{n-1} and after desorption is r_n. Its average value is r_c. Since the capillary is concentric with the pore, the average area of the "capillary" during the desorption which produces Δt_n is equal to A_p x (r_c/r_p). Also $r_c = r_p - t_{r\ w}$here t_r is the thickness of the physically adsorbed layer at the corresponding value of P/P_0. For convenient reference the ratio $r_c/r_p = (r_p - t_r)/r_p$ has been designated by "c." Thus the above equation can be expressed as

$$V_{pn} = Rn\ \Delta Vn - \Delta t_n \sum_{j=1}^{n-1} A_{pj} c_j$$

Equation above provides a practical basis for the computation of pore volume distributions with respect to pore radii. It depends only on the two fundamental assumptions that: (1) the pores are cylindrical (more precisely that pore volume and capillary volume are related to each other as the square of some adequate measure of their cross sections), and (2) that the amount of adsorbate in equilibrium with the gas phase is retained by the adsorbent by two mechanisms:

(a) physical adsorption on the pore walls, and

(b) capillary condensation in the inner capillary volume.

To make the above equation it is necessary to obtain a functional relationship between P/P_0 and Δt. Values of r_k were computed from the classical Kelvin equation.

$$\log (P/P_0) = -4.14/r_k$$

Values of t as a function of the relative pressure were obtained from a plot of the experimental data used by Shull as $r_p = r_k + t$ the addition of the two curves yields the relationship between r_p and the relative pressure. In the equation of V_{pn} it should be noted that r_p and r_k corresponding to it, are used whereas the Δt and

the ΔV are the actual increments corresponding to the decrease in the relative pressure. To simplify and accelerate computation, values of $R = r_p^2/(r_k + \Delta t)^2$ were calculated as functions of r_p for pore radius increments of 10 Å. from 10 to 300 Å. of 5 Å. from 10 to 200 Å. and of 1 Å. From 7 to 25 Å. The results of these calculations are given in Table 6, which constitute the actual working data of the procedure.

Table – 6

S.No	P/P_0	r_p	t	$\bar{r}_p$	Δt	$\bar{r}_k$	R
1	0.165	10	4.74	12.5	1.21	7.1	2.318
2	0.332	15	5.95	17.5	1.02	11.0	2.120
3	0.488	20	6.97	22.5	0.89	15.1	1.980
4	0.927	140	16.61	142.5	0.18	125.7	1.281
5	0.930	145	16.79	147.5	0.175	130.5	1.274
6	0.932	150	16.97	152.5	0.17	135.4	1.265
7	0.947	190	18.25	192.5	0.14	174.2	1.219
8	0.949	195	18.39	197.5	0.14	179	1.215
9	0.950	200	18.52	-	-	-	-

Numerical values of required functions of P/P_0 when $\Delta r = 5$Å

Chapter 2

Experimental Methods and Results

2.1 Experimental Setup

The schematic of the experimental analysis is shown below

Figure - 12

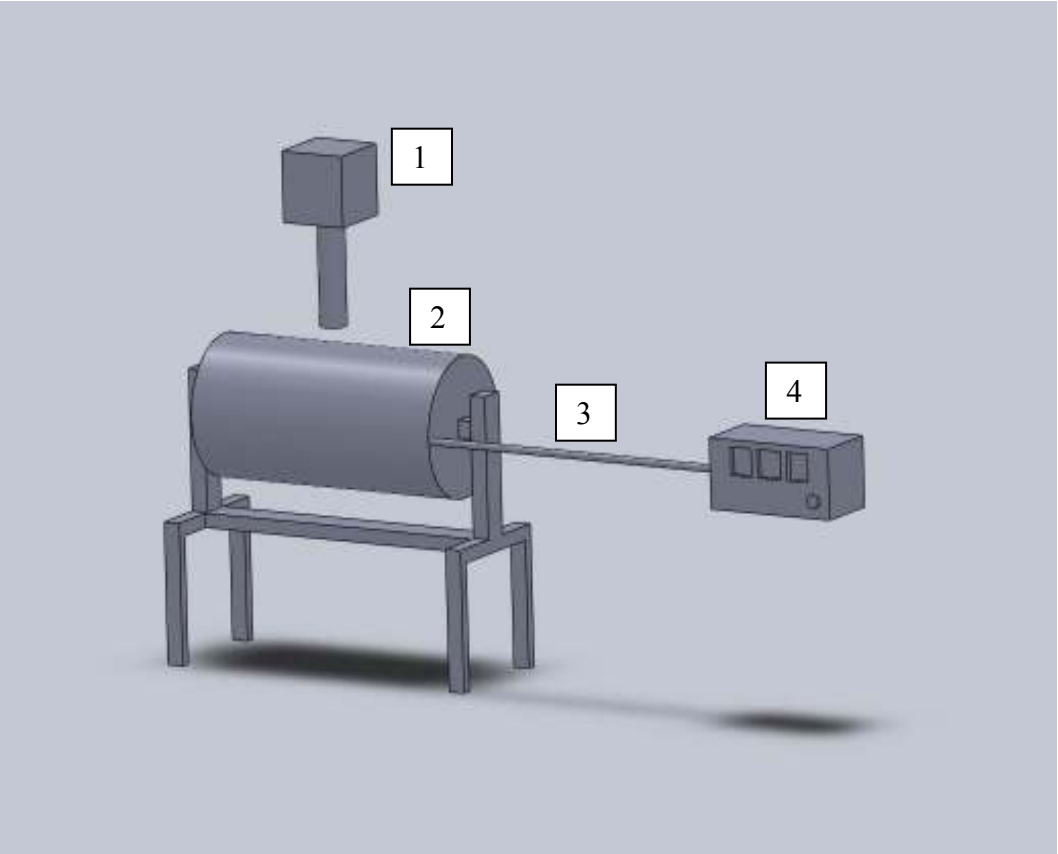

Schematic of experimental setup

1 – Heat Source (Propane Flame)

2 – Reactor

3 – Thermocouple

4 – Temperature Display

The experimental procedure involves burning pyro-gel in a pre-heated reactor. Two experimental setups were used for this purpose:

1. Rectangular Reactor:

Figure - 12

Rectangular reactor

The setup consists of a fabricated brass rectangular block with silica glass covering as shown in the figure. The top face of the block has a cylindrical chamber for the solid fuel and four openings along the circumference to allow restricted amount of oxygen into chamber. The grooves are also be used as a provision to place a thermo couple to obtain the temperature of the burning fuel.

2. Cylindrical Reactor

Figure - 13

Cylindrical Reactor

The setup consists of a cylindrical chamber made of fused silica with two rotary bearings at the end fixed to stand as shown in the figure. The rotary bearings are intended to accommodate an electric motor setup for the rotation of the cylinder if needed in the future work. A thermocouple is placed with its tip inside the cylinder to measure the temperature of the burning fuel. The cylinder is partially sealed to the bearings so as to allow restricted oxygen flow into the burning chamber.

2.2 Experimental Procedure

The experimental procedure for both the reactor setups is very similar. The procedure is described in the following steps

1. Pre-heat the chamber to a required temperature using a heat source, an oxy-propane torch.

2. Add the pyro-gel into the burning chamber with the heat source adding heat to the chamber

3. Obtain temperature readings at various time intervals. The temperature readings were recorded at an interval of 30 seconds for the first reactor setup and at an interval of 15 seconds for the second.

4. The heat source is stopped when the pyro-gel becomes a black residue.

5. The maximum temperature of the burned pyro-gel and time taken to finish the burning process is noted.

2.3 Experimental Results

1. Reactor – 1:

For experimental setup 1, seven experiments were performed at varying pre-heat conditions. The experiments usually lasted about 150 – 180 seconds before the pyro-gel converted into black residual mass. The temperature readings and a plot of the temperature profile for the seven experiments during the course of the trial is shown below.

Table – 7

S.No	Pre-heat temperature (K)	Maximum temperature (K)
1	273	716
2	273	730
3	424	745
4	575	752
5	634	756
6	726	774
7	775	815

Maximum temperature values at various pre-heat conditions for reactor - 1

Figure - 14

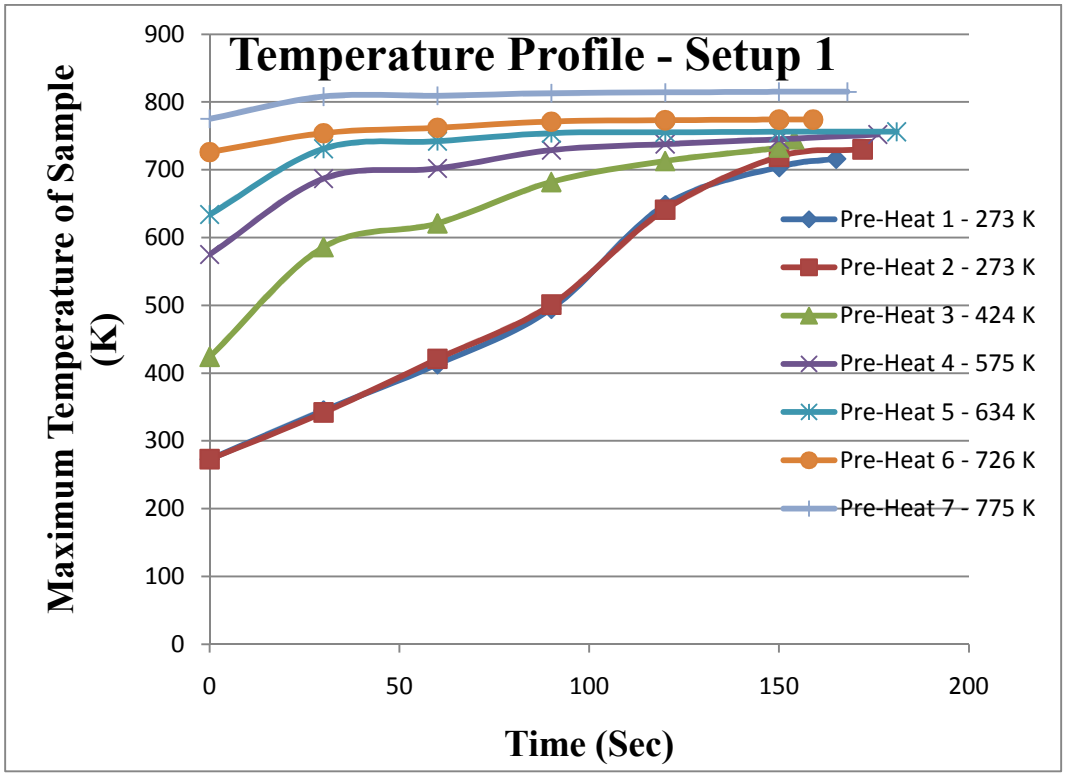

Temperature distribution for reactor - 1

Figures shown below give a picture of the pyro-gel sample after undergoing the heating process.

Figure - 15

Burnt pyro-gel sample in reactor - 1

2. Reactor – 2:

For setup – 2, six experiments were performed at varying pre-heat conditions between 800K to 900 K. The experiments lasted about 90 seconds till black residual mass was obtained. The temperature readings and a plot of the temperature profile during the course of the trial is shown below.

Table – 8

S.No	Pre-Heat Temperature (K)	Maximum Temperature (K)
1	800	906
2	830	931
3	840	948
4	850	961
5	870	967
6	900	997

Maximum temperature values at various pre-heat conditions for reactor-2

Figure - 16

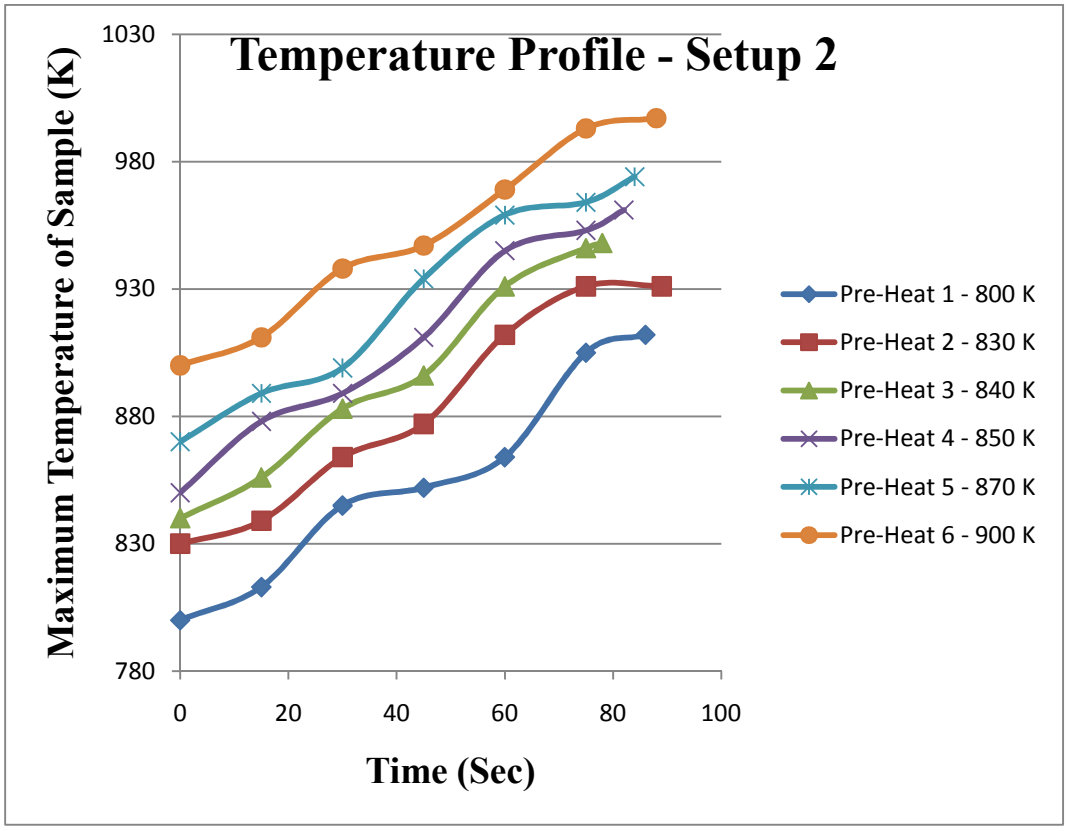

Temperature distribution for reactor – 2

The sequence of figures given below shows the heating process of the fuel sample

Figure - 17

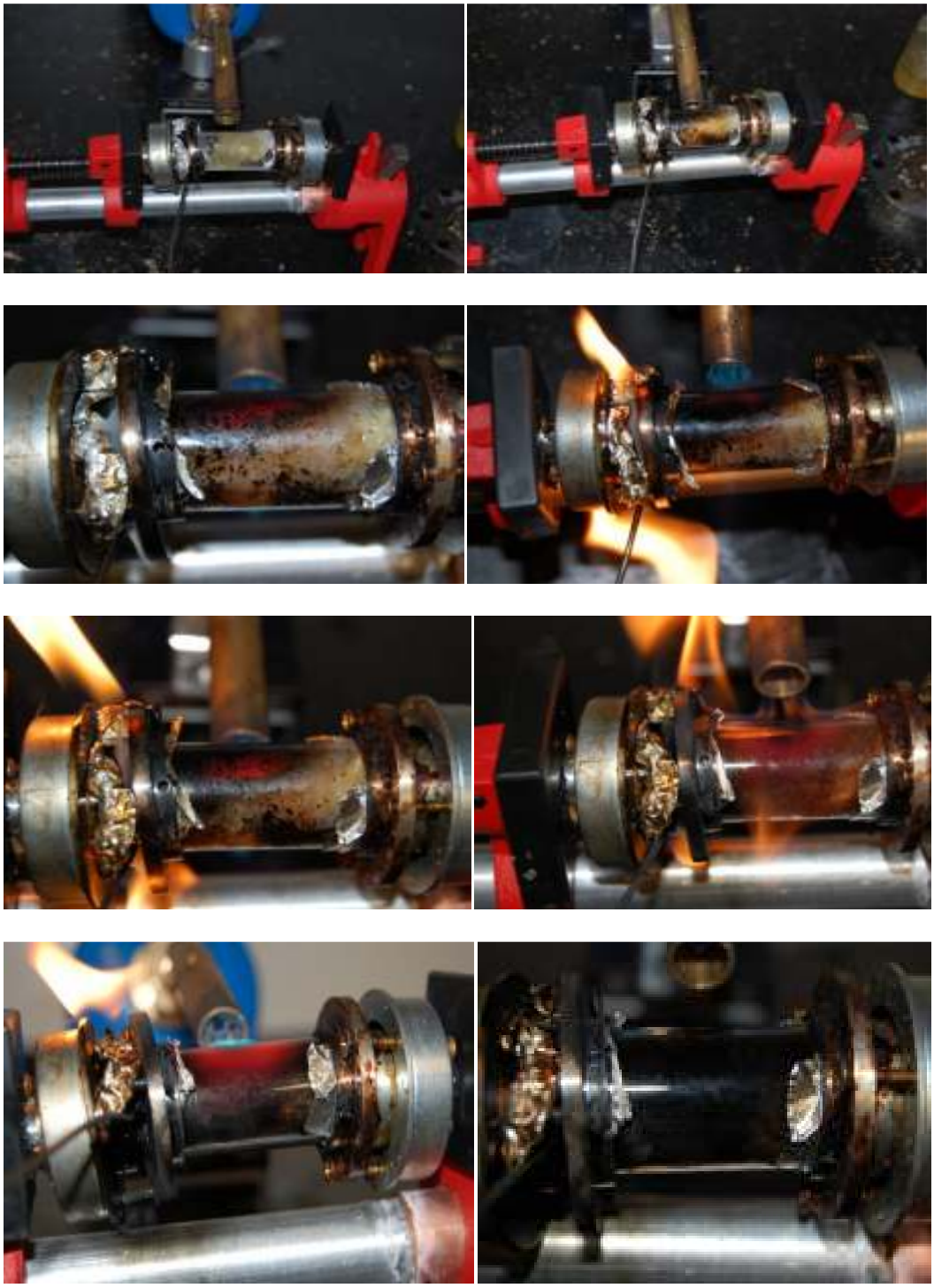

Sequence of experimental process involved in reactor – 2

2.4 Pore Distribution

The carbon residue obtained from the above experiment is then slowly burned for about 12 hours to obtain a white colored sample void of carbon content. Micrometrics ASAP 2000 is used to perform BET/BJH analysis on the white sample to obtain the pore volume to the pore width distribution. The pore volume of the samples varies according to the pre-heat conditions used in the experimental trials. The plot below shows the pore distribution of a few pre-heat conditions.

Figure - 18

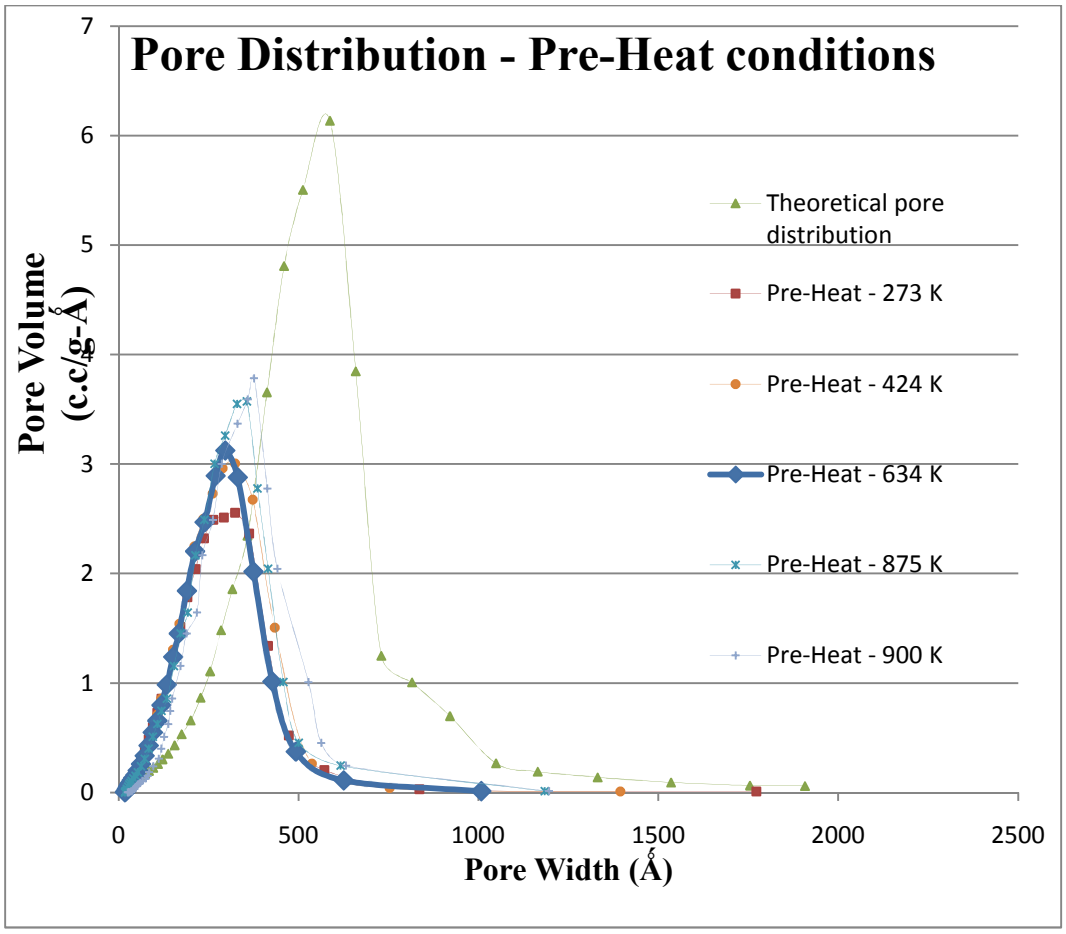

Pore distribution of pyro-gel at various pre-heat conditions

Another experimental analysis was performed for a pre-heat condition of 900 K where the mass of fuel used inside the cylindrical chamber was varied from 5 – 23 grams. Shown below is a plot of the pore distribution.

Figure – 19

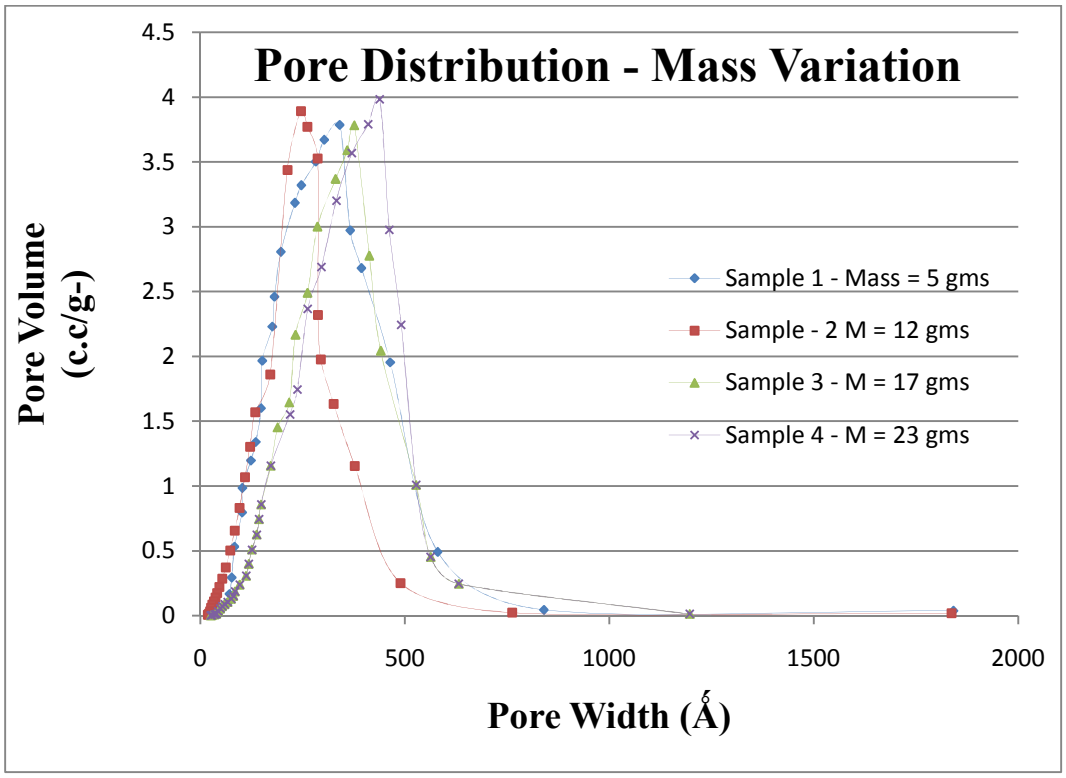

Pore distribution of pyro-gel at various input masses

2.5 Discussion:

The temperature profile for the experimental setup – 1 is not conclusive regarding any process, but the temperature profile for setup – 2 shows there is a steep rise in the temperature in the initial stages, then the temperature has a slow gradual increase until it reaches the steady state where the temperature remains constant. This is a valid trend because, during the initial stages of the experiment there will be some small scale explosions inside the fuel chamber contributing to rapid rise in temperature, once the explosions stop, temperature rise is going to be gradual and when all the fuel inside the chamber is used, only contributing factor to the temperature rise is the heat supplied and the setup is going to eventually reach steady state at the maximum temperature.

The pyro-gel when subjected to heat undergoes the following reactions

$4\ AlOOH + O_2 \rightarrow 2\ Al_2O_3 + 2\ H_2O$

C – H bonds + limited $O_2 \rightarrow$ C – C bonds + H_2O

C – H bonds + excess $O_2 \rightarrow CO_2 + H_2O$

The above equations give an insight into the optimum conditions at which the fuel needs to be burned. The boiling point of Al_2O_3 is 313 ^{0}C. If the fuel is burned at an initial temperature close to boiling point, we have what is called as a capillary effect. If Al_2O_3 starts boiling then vapors create capillary suction on the walls of the pores thus compressing them and reducing the pore volume. When the initial temperature of burning is very high (~ 500 ^{0} C) the capillary effect is reduced, retaining the pore size. Burning the fuel in excess oxygen will break the C – H bonds and effect in release of carbon in shape of CO_2. Burning in limited

oxygen will break the C – H bonds, but instead of formation and escape of CO_2, C – C bonds are formed, which provide structural support to the pores and prevents it from collapsing.

Looking at the plots showing the pore distribution, the above explanation looks valid because there is a noticeable increase in the pore volume over a range of pore width with the increase in pre-heat temperature. The percentage increase in the pore volume is **58.33 %**

The fuel chamber for the experimental setup is sealed almost entirely to restrict the oxygen flow. So the mass of the fuel in the fuel chamber is inversely proportional to the amount of initial oxygen available for the burning of the fuel. But the plot of pore distribution vs. mass variation doesn't show any noticeable increasing trend with the increase in the mass of fuel used with the maximum percentage increase in the pore volume being **8.11 %**

Chapter 3

Computational Methods and Results

The experimental process explained above is simulated in FLUENT using a Finite Rate Chemistry Eddy-Dissipation model in unsteady state. Two models were used to accurately simulate the experimental process

1. Non pre-mixed model

2. Porous model

3.1 Non pre-mixed model

Figure - 20

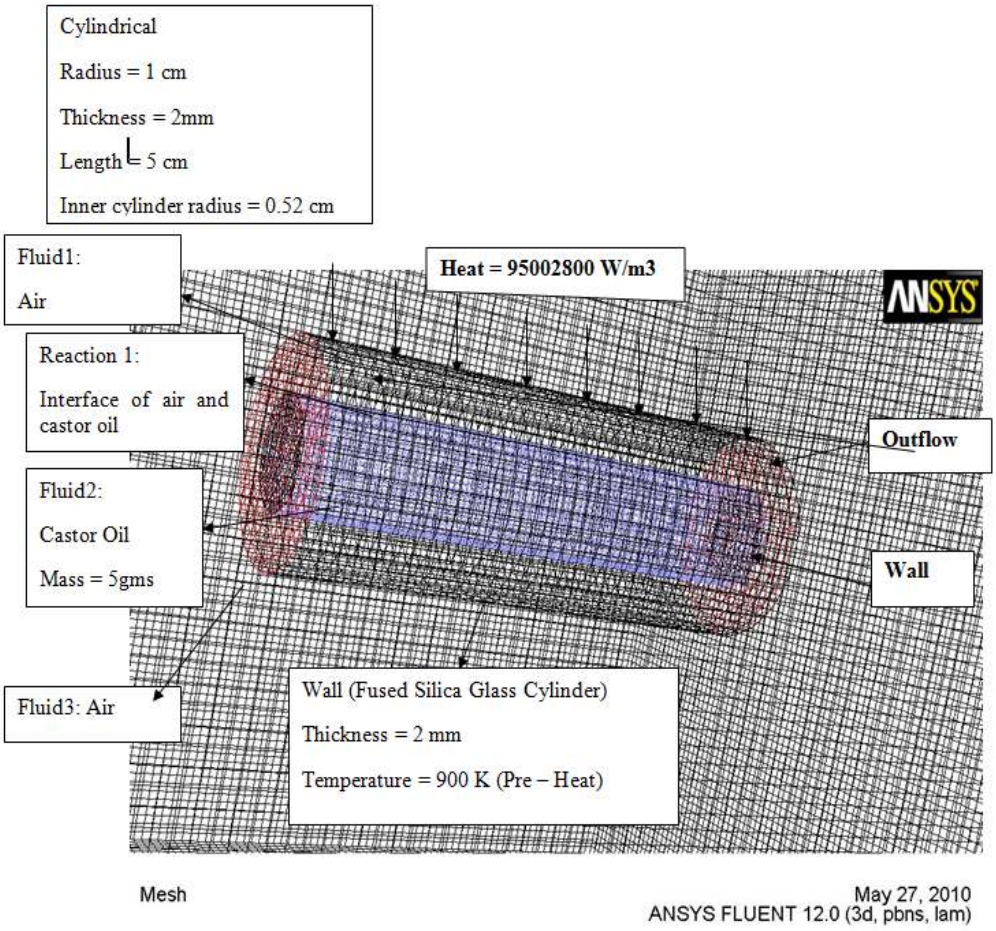

Non-premixed model for pyro-gel experimental analysis

Figure - 21

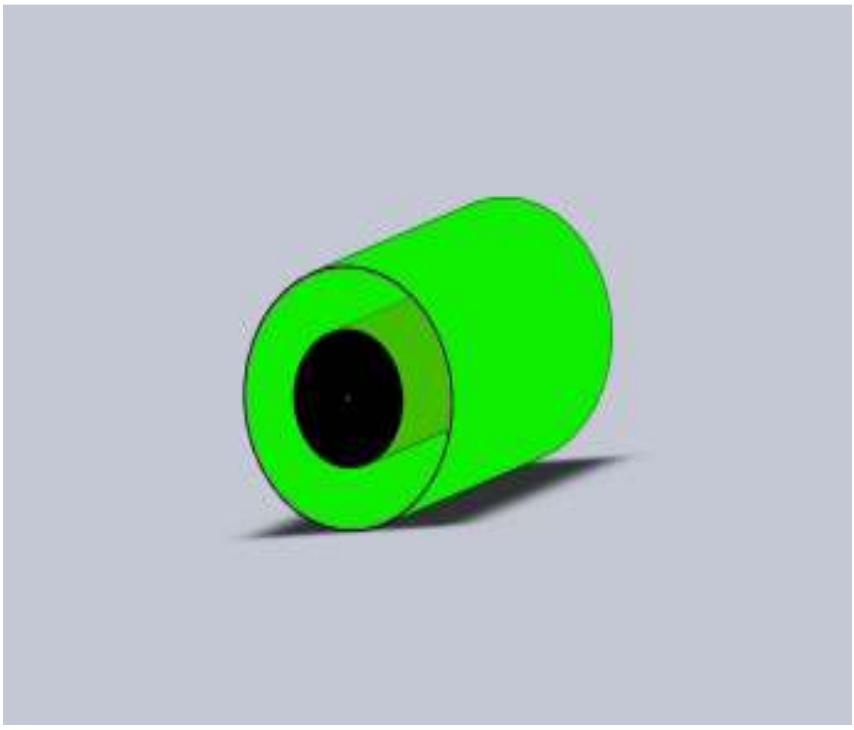

Geometric representation of non-premixed model for pyro-gel experimental analysis

This model consists of a cylindrical mesh of dimensions same as the cylinder used in the experiment placed in a large volume consisting of air. The interior of the cylinder contains a smaller cylinder filled with the solid pyro-gel. The surrounding of the cylinder contains air. The size diameter of the smaller cylinder is obtained as follows

Mass of fuel = 5 gms

Density = 961 kg/m^3

Volume of small cylinder= $5.2029 \times 10^{-6}\ m^3$

Volume of Reactor = $\prod (r-t)^2 \times L = \prod \times 0.008^2 \times 0.05 = 1.005 \times 10^{-5}\ m^3$

Diameter of inner cylinder

= Diameter of the reactor x direct ratio of the volumes = 1.04 cm

The model involves finite rate volumetric reaction at the interface of the fluid species Ricinoelic acid $C_{18}H_{34}O_3$ and oxygen.

$C_{18}H_{34}O_3 + 25\ O_2 \rightarrow 18\ C0_2 + 17\ H_2O$

Rate equation $R = 4.836*10^9\ [C_{18}H_{34}O_3]^{0.1}\ [O_2]^{1.65}$

Activation energy = 1.256×10^5 KJ/kgmol

Ricinoelic acid is the main component in castor oil (95%), so the model becomes simplified by assuming a single reaction between Ricinoelic acid and oxygen.

Shown below is the maximum temperature profile obtained in the simulation and in comparison with the experimental data.

Table – 9

S.No	Pre-Heat Temperature (K)	Maximum Temperature Non-Premixed model (K)	Maximum Temperature Experiment (K)
1	800	929	906
2	830	959	931
3	840	984	948
4	850	1001	961
5	870	1012	967
6	900	1030	997

Temperature distribution comparison between experiment and non-premixed model

Figure - 22

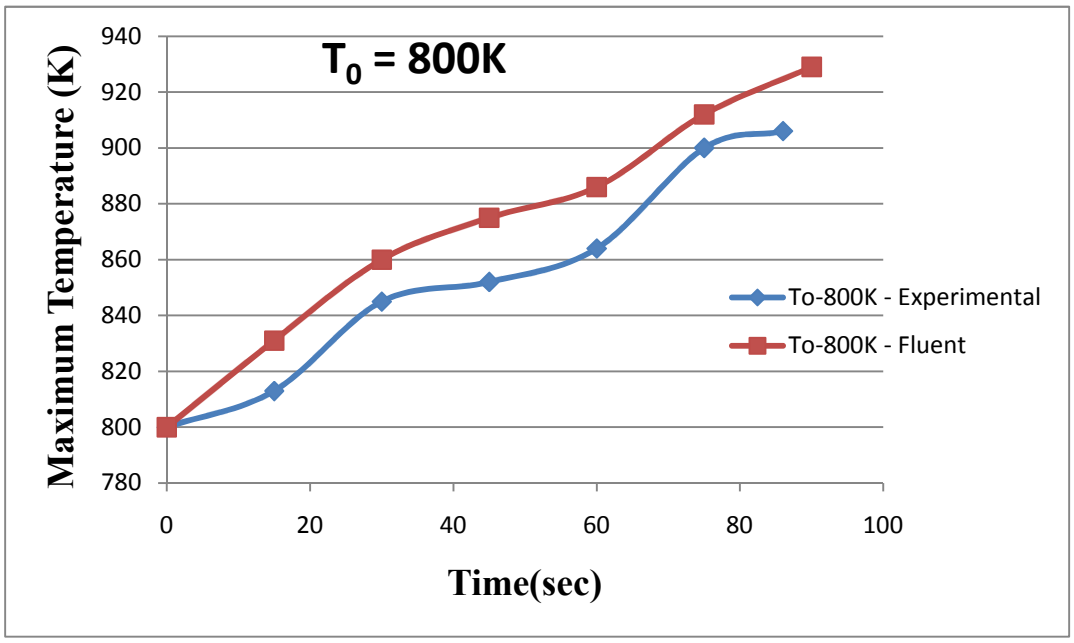
T_0 = 800K
Maximum Temperature (K)
940
920
900
880
860
840
820
800
780
0
20
40
60
80
100
Time(sec)
To-800K - Experimental
To-800K - Fluent

(a)

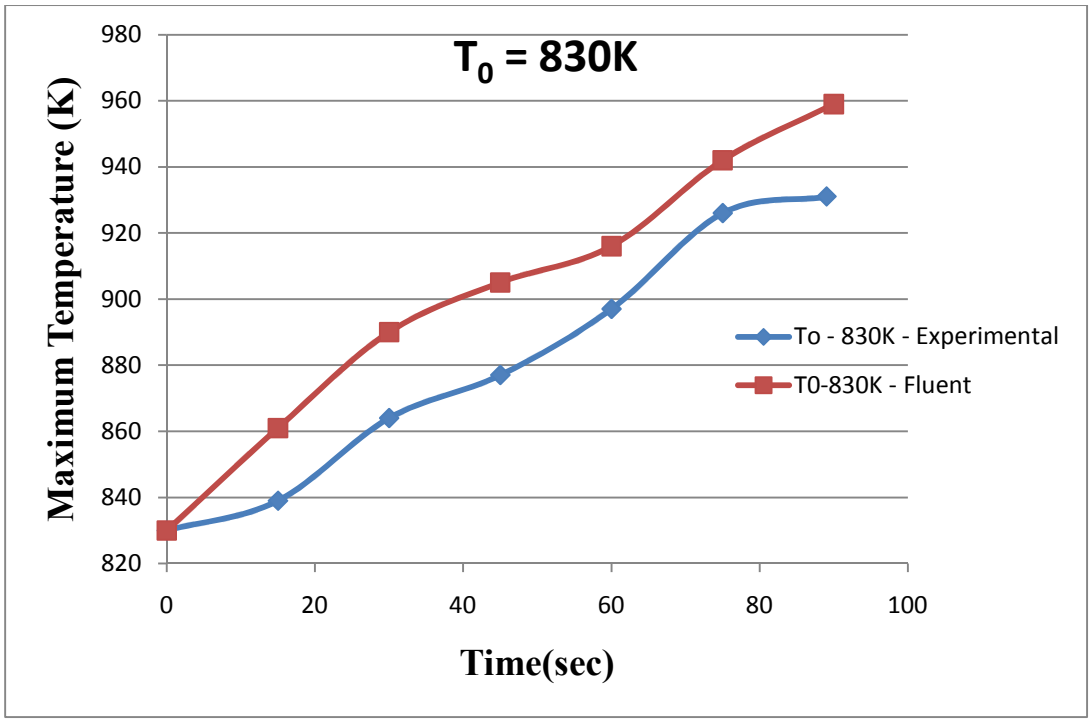
T_0 = 830K
Maximum Temperature (K)
980
960
940
920
900
880
860
840
820
0
20
40
60
80
100
Time(sec)
To - 830K - Experimental
T0-830K - Fluent

(b)

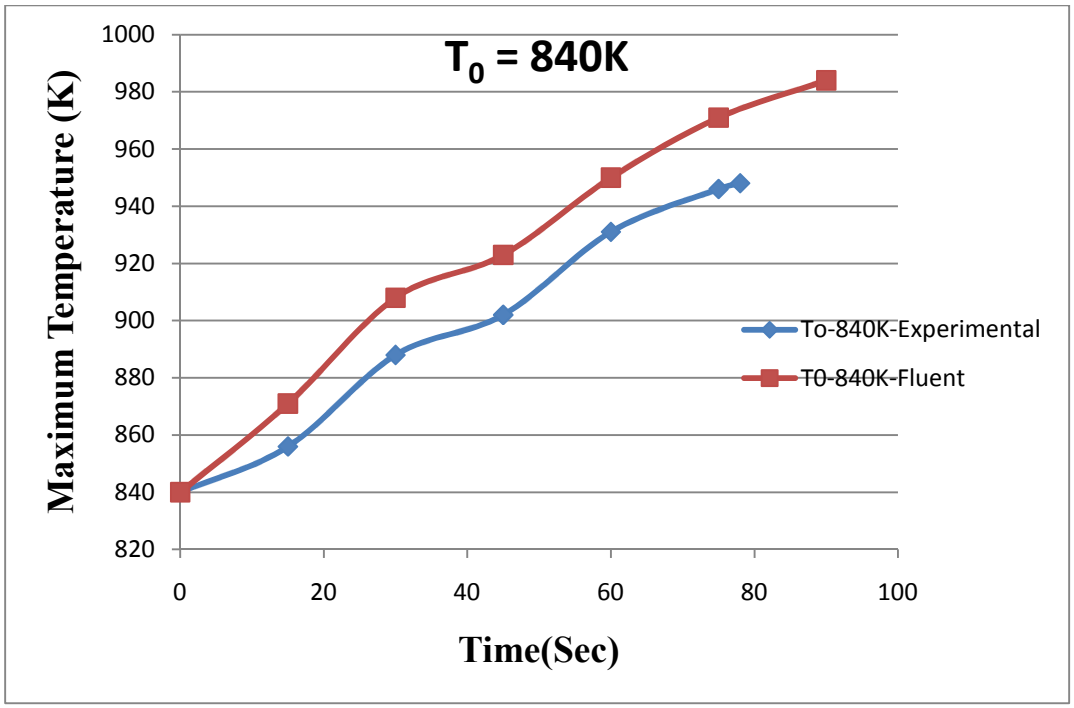
T0 = 840K
Maximum Temperature (K)
1000
980
960
940
920
900
880
860
840
820
0
20
40
60
80
100
Time(Sec)
To-840K-Experimental
T0-840K-Fluent

(c)

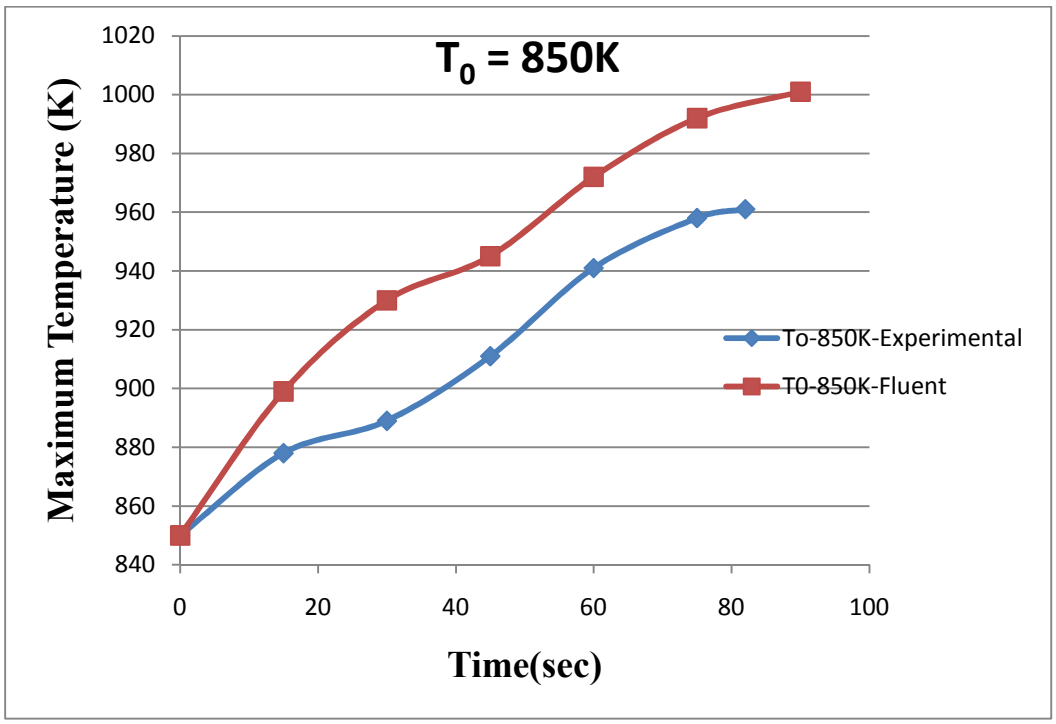
T0 = 850K
Maximum Temperature (K)
1020
1000
980
960
940
920
900
880
860
840
0
20
40
60
80
100
Time(sec)
To-850K-Experimental
T0-850K-Fluent

(d)

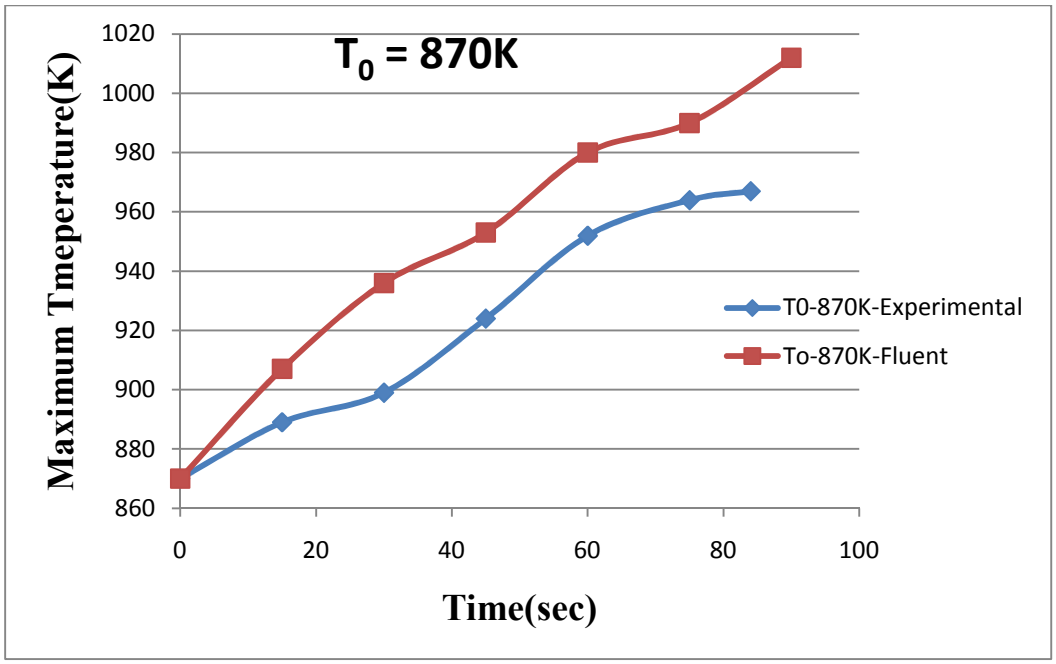

(e)

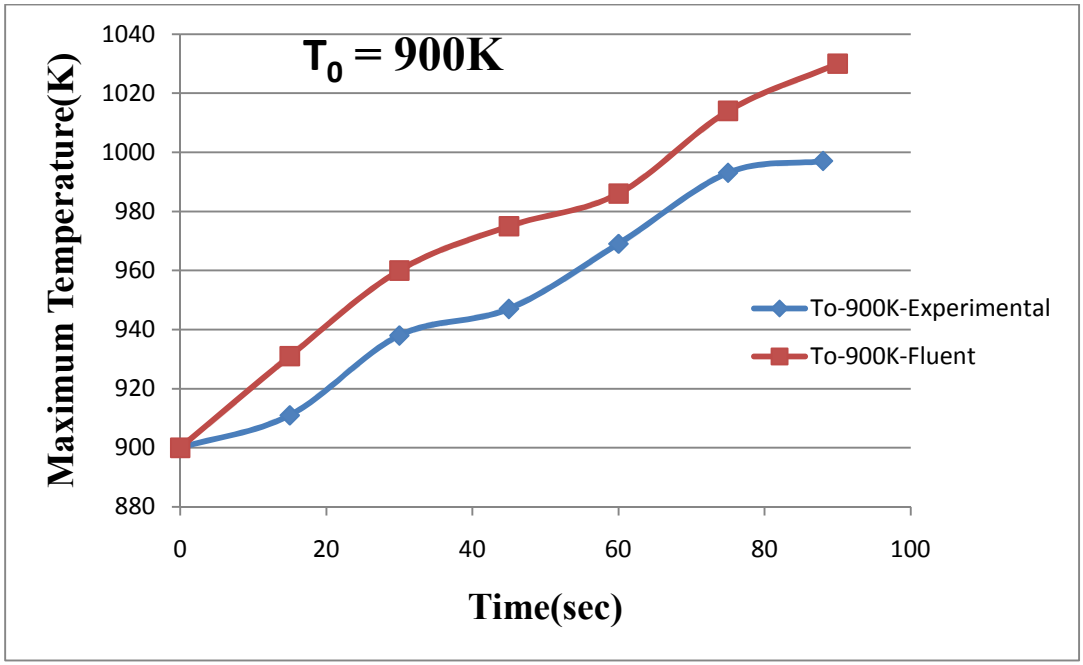

(f)

(a-f) Temperature distribution comparison between experiment and simulation at various pre-heat conditions

3.2 Porous model

Figure - 23

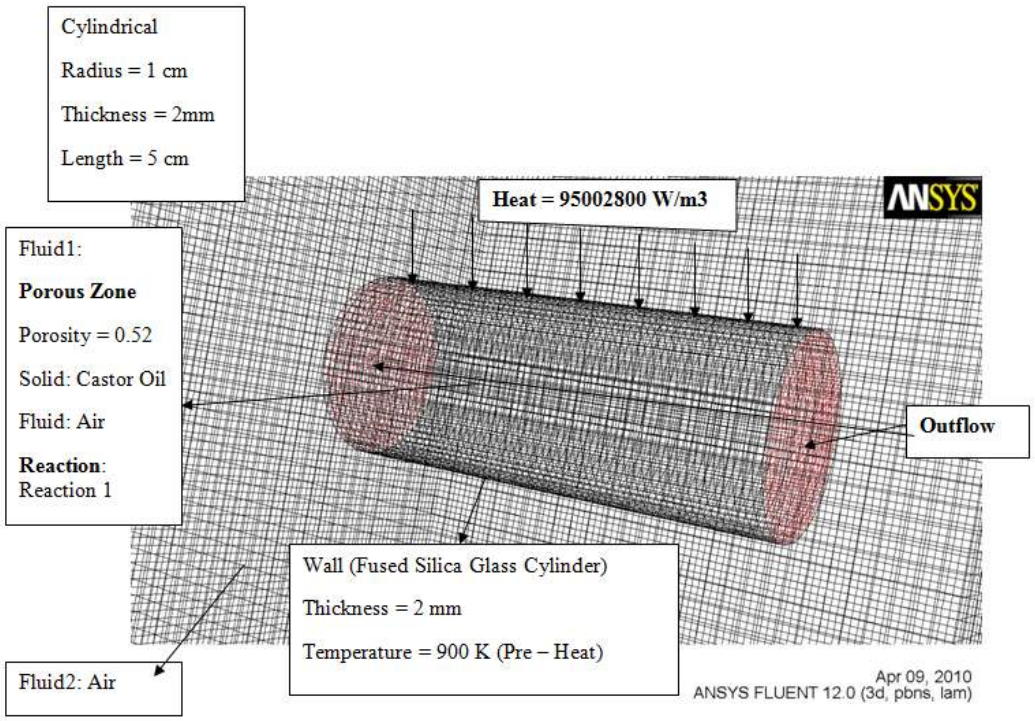

Porous model for pyro-gel experimental analysis

Figure - 24

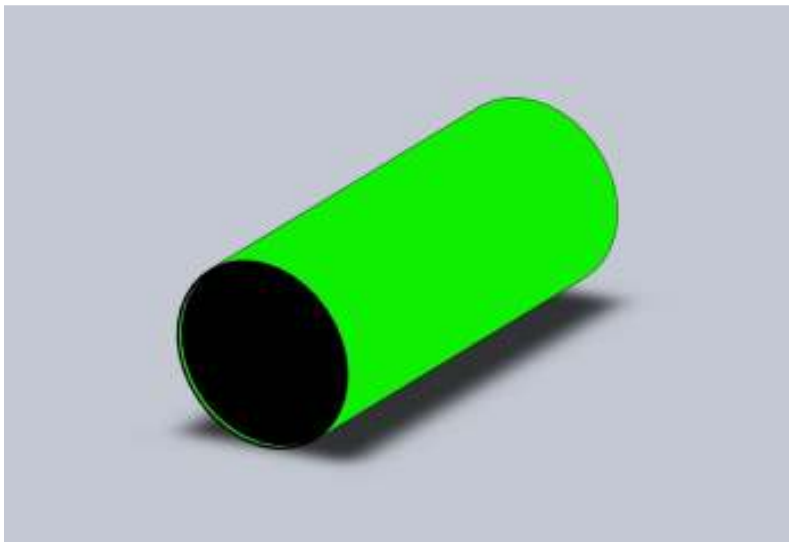

Geometric representation of porous model for pyro-gel experimental analysis

This model consists of a cylindrical mesh of dimensions same as the cylinder used in the experiment placed in a large volume consisting of air. The interior of the cylinder contains a mixture of Castor Oil (Primary fuel in the solid fuel) and air. The porosity of the mixture is obtained as shown below.

Mass of fuel = 5 gms

Density = 961 kg/m^3

Volume = $5.202 \times 10^{-6}\ m^3$

Volume of Cylinder = $\prod (r-t)^2 \times L = \prod \times 0.008^2 \times 0.05 = 1.005 \times 10^{-5}\ m^3$

Porosity = Volume of fuel/Volume of cylinder = 0.52

The model uses finite rate chemistry surface reaction of solid species Ricinoelic Acid $C_{18}H_{34}O_3$ (Primary component in castor oil) with air. Initial simulation used the reaction of Ricinoelic acid with oxygen

$C_{18}H_{34}O_3 + 25\ O_2 \rightarrow 18\ C0_2 + 17\ H_2O$

Rate equation $R = 4.836*10^9\ [C_{18}H_{34}O_3]^{0.1}\ [O_2]^{1.65}$

Activation energy = 1.256×10^5 KJ/kgmol

The above equation does not truly reflect the experimental process, so the reaction was modified to accommodate Nitrogen as an inert gas, since there is very little information available about the effect of nitrogen on castor oil as well as on rate equation and activation energy.

$C_{18}H_{34}O_3 + 25\ O_2 + 93.18\ N_2 \rightarrow 18\ C0_2 + 17\ H_2O + 93.18\ N_2$

(Air – N_2/O_2 ratio = 78.09/20.95 = 3.727)

Rate equation $R = 4.836*10^9\ [C_{18}H_{34}O_3]^{0.1}\ [O_2]^{1.65}\ [N_2]^0$

Activation energy = 1.256 x 10^5 KJ/kgmol

The porosity model is a more realistic in representing the experimental model compared to the non-premixed model.

Shown below is the maximum temperature profile of both the reactions and in comparison with the experimental data.

Table – 10

S.No	Pre-Heat Temperature (K)	Maximum Temperature - O_2 (K)	Maximum Temperature – Air (K)	Maximum Temperature – Experiment (K)
1	900	1024	1010	997

Porous Model – Maximum temperature for models with O_2 and Air

Figure – 25

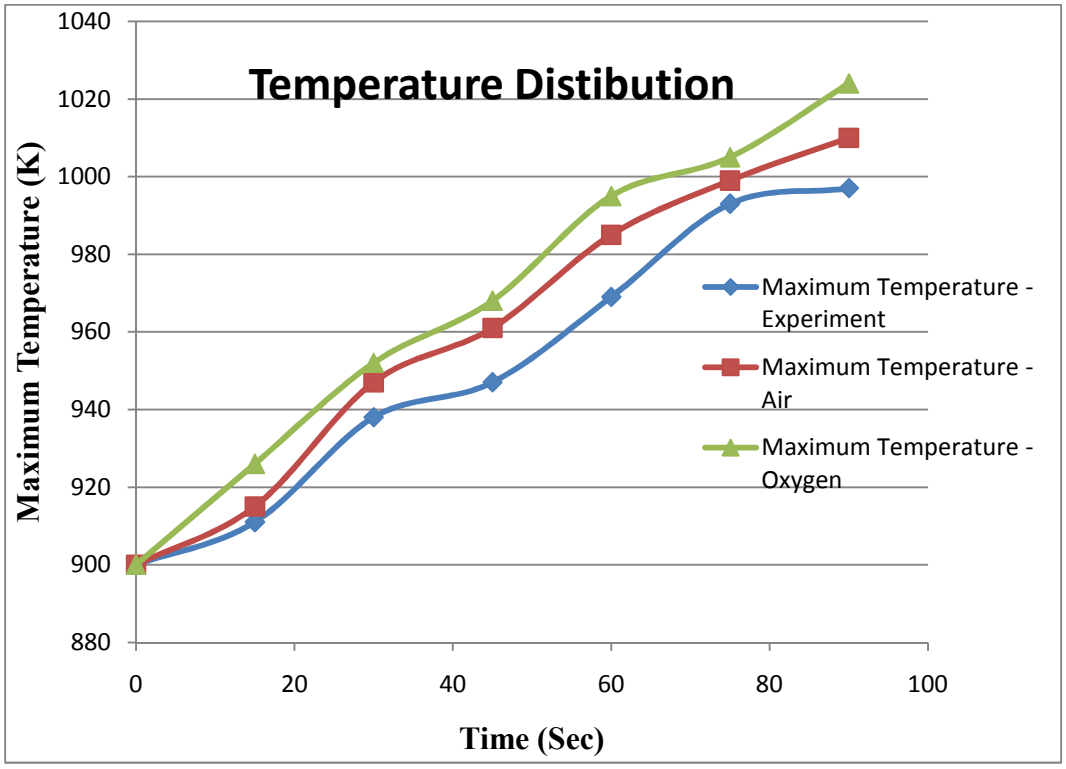

Temperature distribution comparison between experimental and simulation involving oxygen and air at 900K pre-heat temperature

Table – 11

S.No	Pre-Heat Temperature (K)	Maximum Temperature – Porous Model (K)	Maximum Temperature – Experiment (K)
1	800	924	906
2	830	954	931
3	840	979	948
4	850	994	961
5	870	996	967
6	900	1024	997

Figure - 26

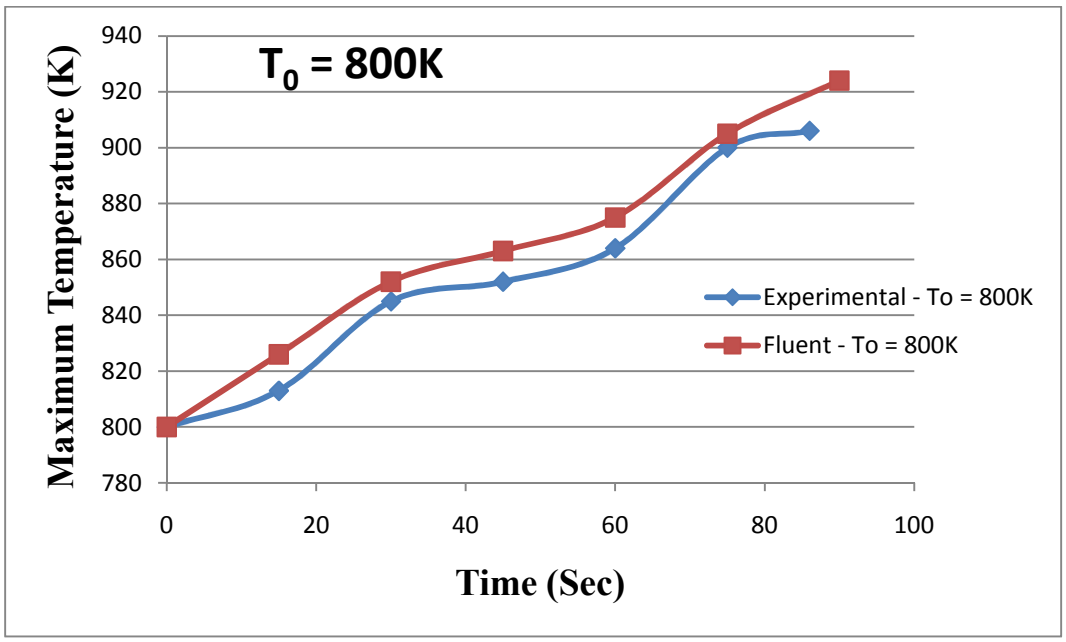

(a)

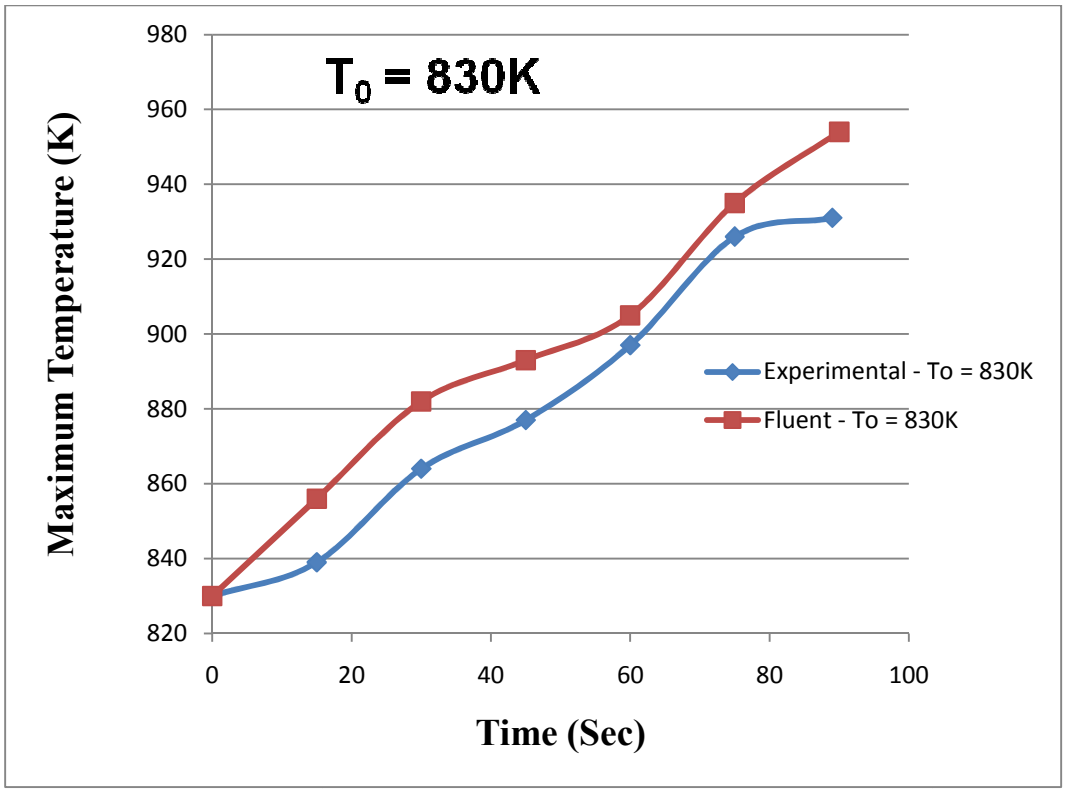
T_0 = 830K
Maximum Temperature (K)
980
960
940
920
900
880
860
840
820
0
20
40
60
80
100
Time (Sec)
Experimental - To = 830K
Fluent - To = 830K

(b)

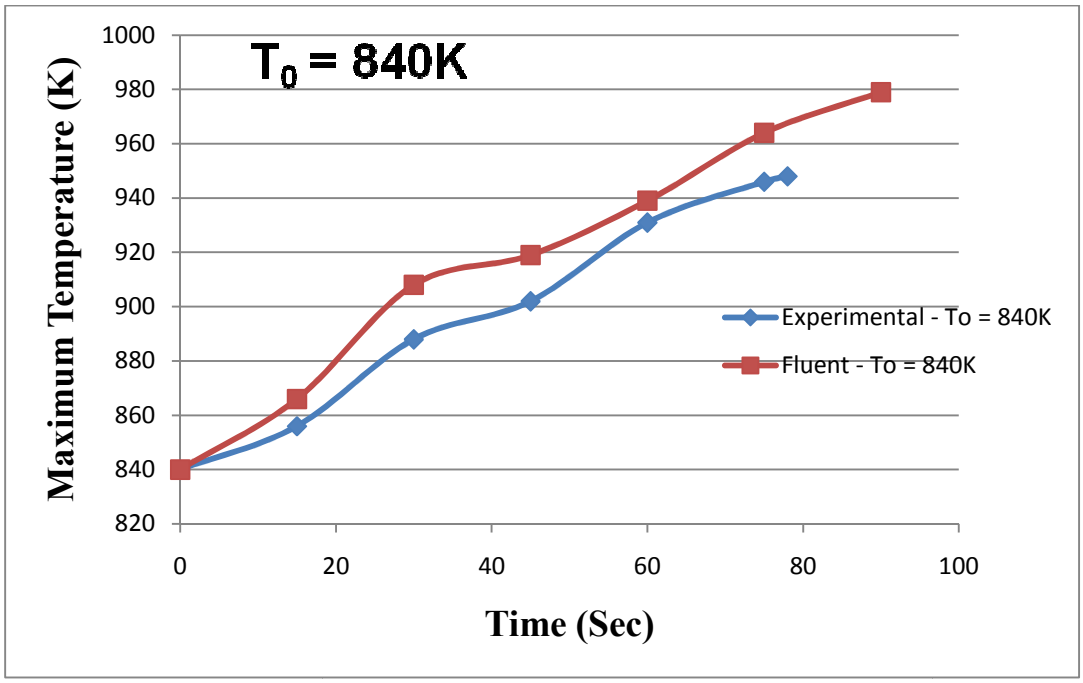
T_0 = 840K
Maximum Temperature (K)
1000
980
960
940
920
900
880
860
840
820
0
20
40
60
80
100
Time (Sec)
Experimental - To = 840K
Fluent - To = 840K

(c)

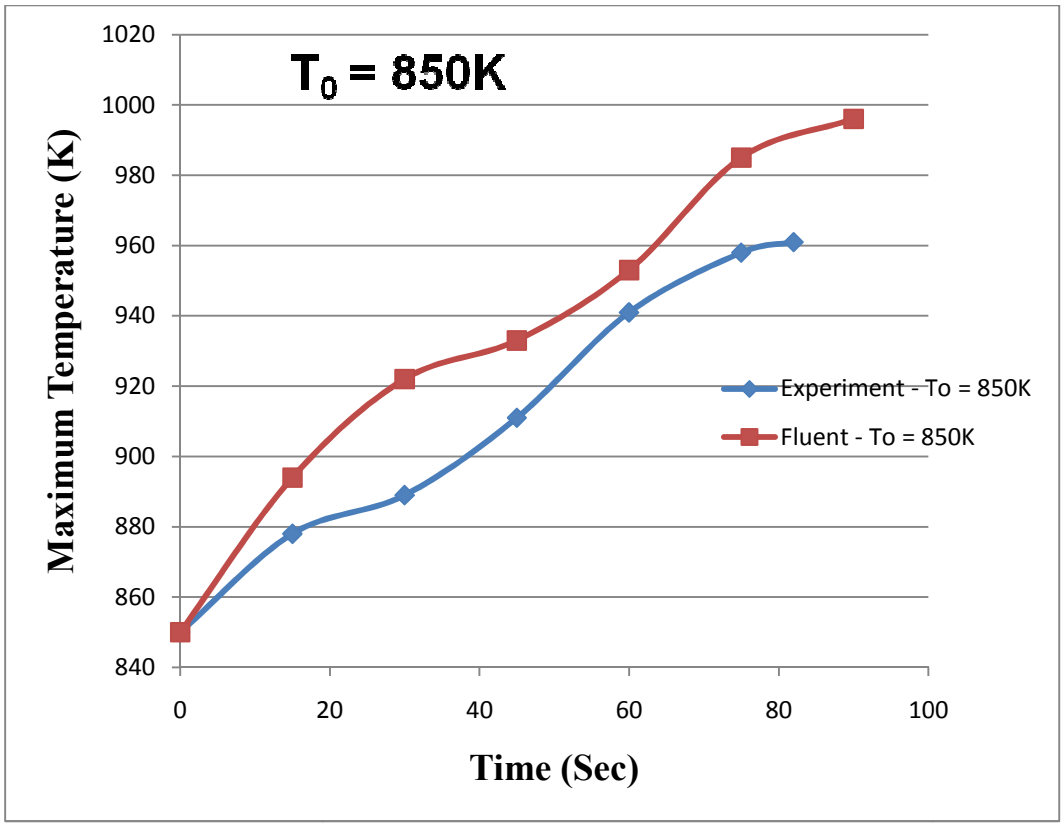
T0 = 850K
Maximum Temperature (K)
1020
1000
980
960
940
920
900
880
860
840
0
20
40
60
80
100
Time (Sec)
Experiment - To = 850K
Fluent - To = 850K

(d)

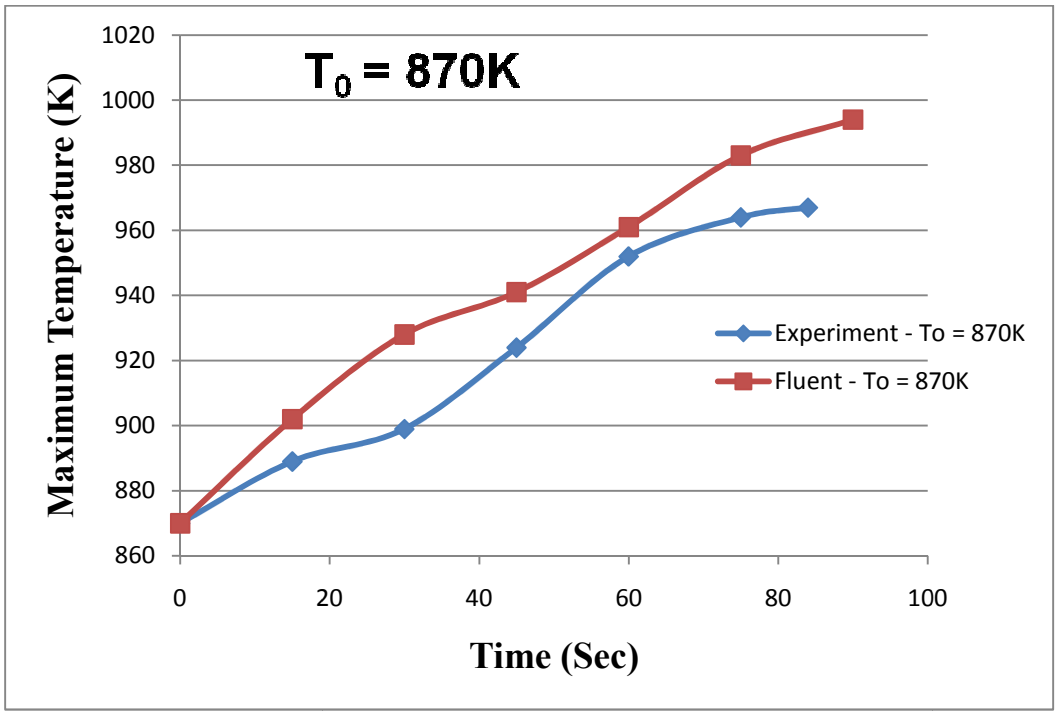
T0 = 870K
Maximum Temperature (K)
1020
1000
980
960
940
920
900
880
860
0
20
40
60
80
100
Time (Sec)
Experiment - To = 870K
Fluent - To = 870K

(e)

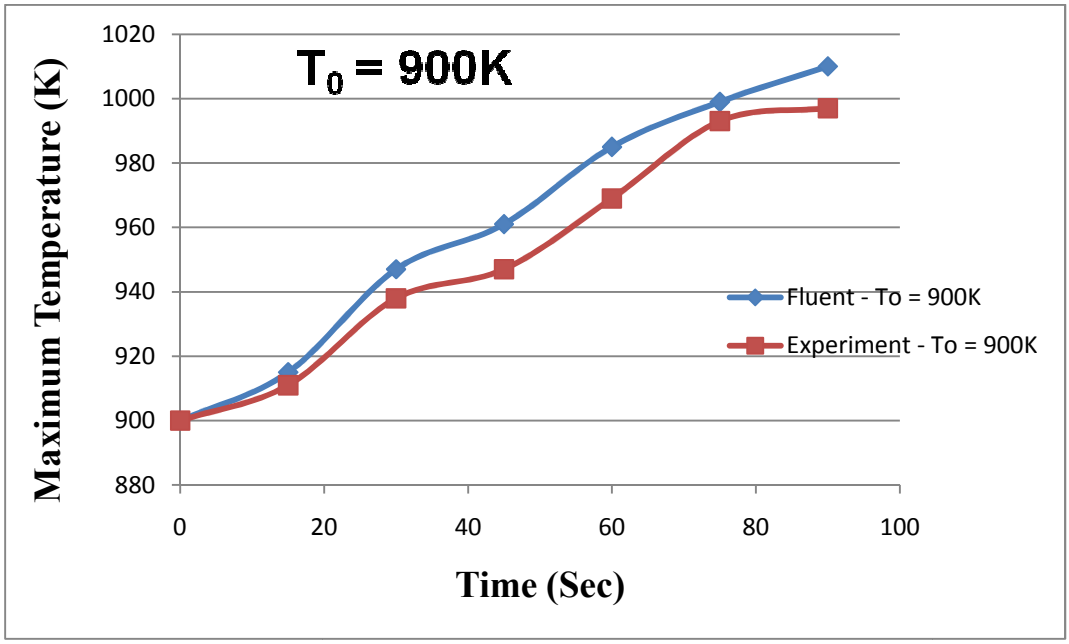

(f)

(a-f) Temperature distribution comparison between experiment and simulation at various pre-heat conditions

3.3 Discussion

The first model uses a non-premixed two cylinder mesh with the inner cylinder filled with fuel and the outer cylinder with oxygen. The temperature profiles obtained at different pre-heat conditions are compared to the temperature profiles from the experimental analysis. The maximum temperature obtained from the model is about **2 – 3%** more than the maximum temperature from the experimental analysis. This can be attributed to a small heat loss due to leakage in the experimental setup compared to no heat loss in the simulation model. Also the temperature profile follows a close pattern with the experimental analysis, i.e. initial rapid rise in temperature during the initial stages and steady small rise in temperature during the middle and final stages of burning.

The second model uses a pre-mixed porous mesh with fuel and oxygen inside the cylinder. As in the first model the temperature profiles are obtained at different pre-heat conditions and compared to the temperature profiles from the experimental analysis. The maximum temperature obtained from this model is much closer to the maximum temperature obtained from experimental analysis falling in the **1.5 – 2%** range. This can be attributed to higher accuracy of the porous model in comparison to the non-premixed model. The temperature profile follows pattern similar to the first model. Also a simulation was run by using air instead of oxygen for one pre-heat condition and the maximum temperature obtained is less than **1%** higher than the maximum temperature from the experimental analysis.

Chapter 4

Mathematical Model and Results

4.1 Relation for average pore volume

The pore distribution data obtained from experimental analysis shows that the pore volume is directly related to the initial pre-heat temperature. Given below is a simple relation of the average pore volume in relation to the pre-heat temperature

$$\mathbf{V_p\,(T_0) = \alpha + \beta\,T_0 + \gamma\,T_0^2}$$

Where, V_p: Average pore volume

T_0: Pre-heat temperature in ^{0}K

The pore distribution curve can be approximated to a triangle. So the average pore volume is obtained by using the formula given below,

V_p = Area under the curve/pore width range

The table below shows the average pore volume at various pre-heat temperatures

Table - 12

S.No	Pre-heat temperature (K)	Average pore volume (cm^3/g-Å)
1	273	1.25
2	424	1.5
3	634	1.55
4	875	1.75
5	900	1.9

Average pore volume at different pre-heat temperatures

Figure – 27

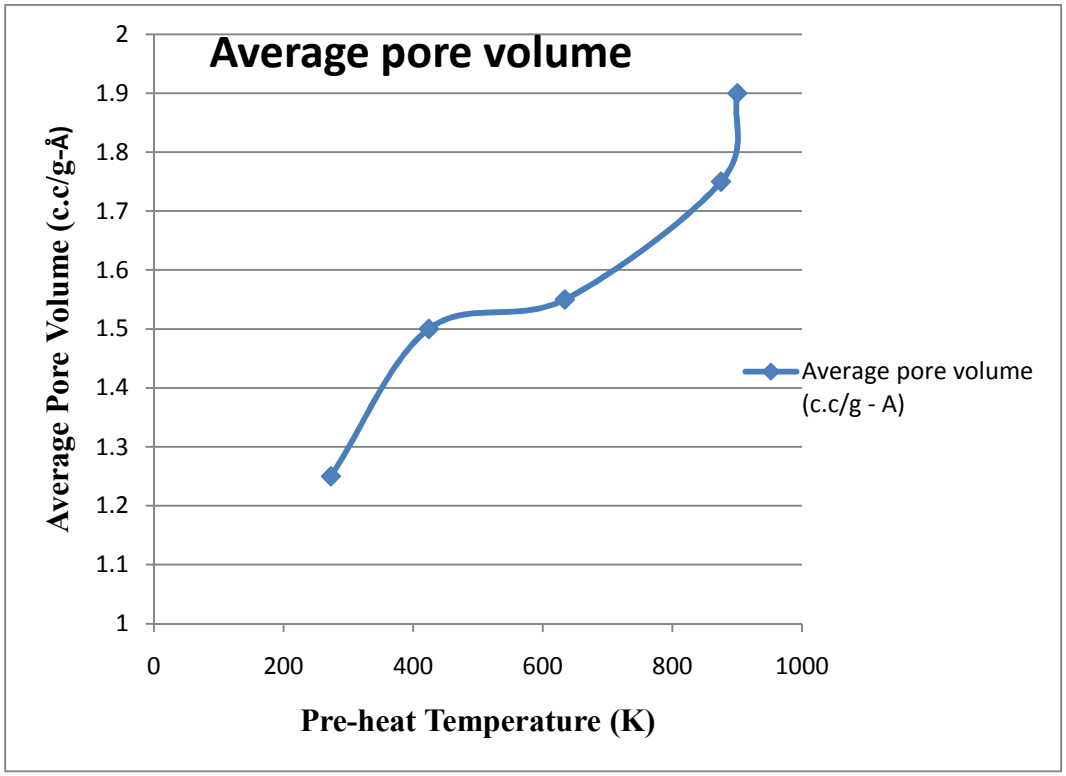

Average pore volume at various pre-heat temperatures

The curve above shows there is a rapid increase in pore volume after 600K. This can be attributed to the pre-heat temperature being much higher than the boiling point of Al_2O_3 which is 584 K.

Algebra analysis is used to obtain a curve fit using the data obtained. The equation is substituted with the experimental data

$$\alpha + 273\,\beta + 74529\,\gamma = 1.25$$
$$\alpha + 424\,\beta + 188356\,\gamma = 1.5$$
$$\alpha + 634\,\beta + 401956\,\gamma = 1.55$$
$$\alpha + 875\,\beta + 765625\,\gamma = 1.75$$
$$\alpha + 900\,\beta + 810000\,\gamma = 1.9$$

The above system of equations can be written in the form of matrices as

$$Ax = b$$

Where, $A = \begin{pmatrix} 1 & 273 & 74529 \\ 1 & 424 & 188356 \\ 1 & 634 & 401956 \\ 1 & 875 & 765625 \\ 1 & 900 & 810000 \end{pmatrix}$, $b = \begin{pmatrix} 1.25 \\ 1.5 \\ 1.55 \\ 1.75 \\ 1.9 \end{pmatrix}$

The curve fit solution for the system of equations is obtained by

$$x = \begin{pmatrix} \alpha \\ \beta \\ \gamma \end{pmatrix} = (A^T A)^{-1} (A^T b)$$

By solving the above expression, $x = \begin{pmatrix} 1.043 \\ 0.000881 \\ -0.3532\ e-9 \end{pmatrix}$

The relation is

$$V_p (T_0) = 1.0505044 + 0.000881\ T_0 - 0.3532\ e^{-9}\ T_0^2 \ \ cm^3/g\text{-Å}$$

4.2 Pore distribution prediction from math model

Elliot Barrett, Leslie Joyner and Paul Halenda proposed a theory for pore distribution based on the formula

$$V_{PD} = \frac{4}{w_b - w_a}\ w_n \int_{w_a}^{w_m} V_P \quad \text{if } w_n < w_m$$

$$= \frac{4}{w_b - w_a}\ (w_n - w_m) \int_{w_m}^{w_b} V_P \quad \text{if } w_n > w_m$$

Where, V_{PD} = Total pore volume (cm^3/g- Å)

(w_a, w_b) = Range of pore width (Å) ~ (0, 2 x w_m)

w_n = pore width corresponding to measured pore volume

w_m = pore width corresponding to maximum pore volume

V_P = average pore volume

The above equation can be modified to a discrete form as

$$V_{PD} = \frac{4}{w_b - w_a} w_n \sum_{i=1}^{m} V_P \text{ if } w_n < w_m$$

$$= \frac{4}{w_b - w_a} (w_n - w_m) \sum_{i=m}^{n} V_P \text{ if } w_n > w_m$$

The above expression can be used to find the pore distribution over a pore width range. The figures below give a comparison between pore distribution obtained from experimental analysis and the equation

Figure - 28

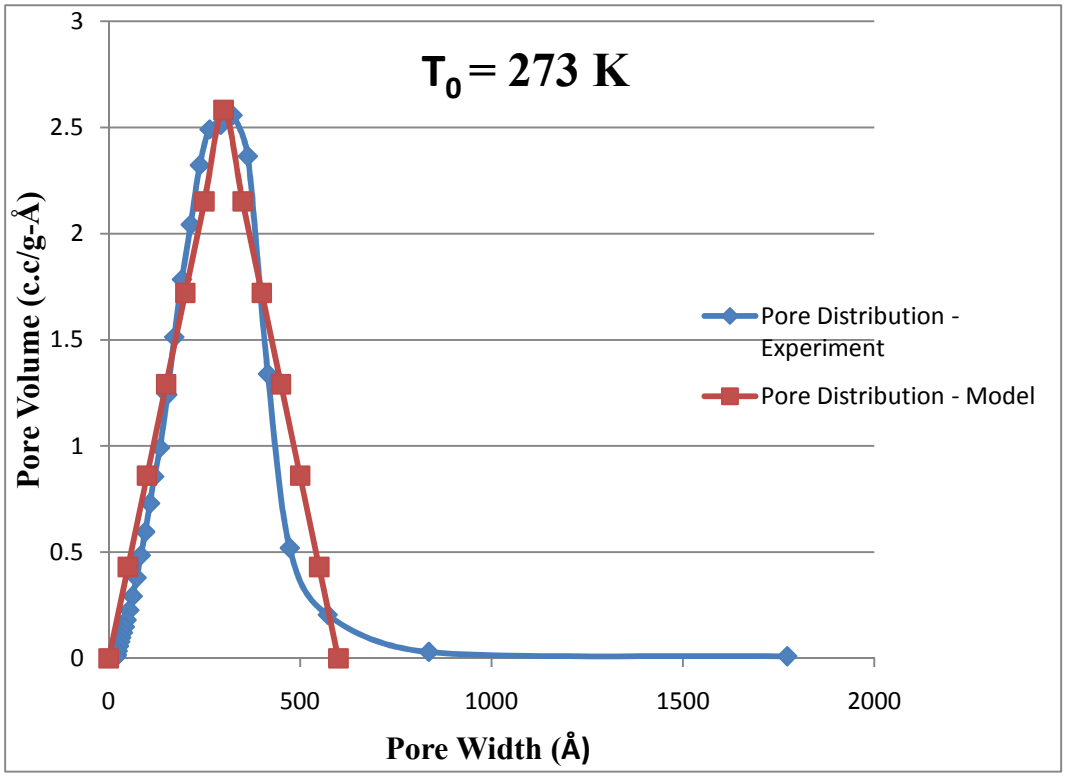

(a)

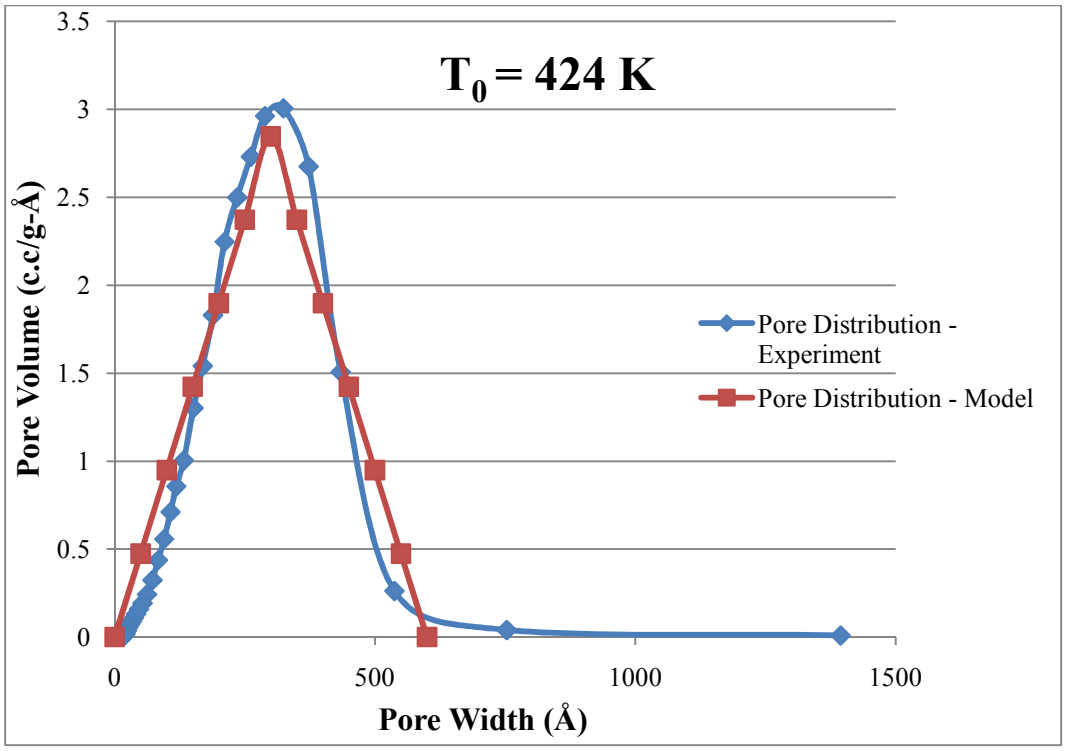
T0 = 424 K
Pore Volume (c.c/g-Å)
Pore Width (Å)
Pore Distribution - Experiment
Pore Distribution - Model
0
0.5
1
1.5
2
2.5
3
3.5
0
500
1000
1500

(b)

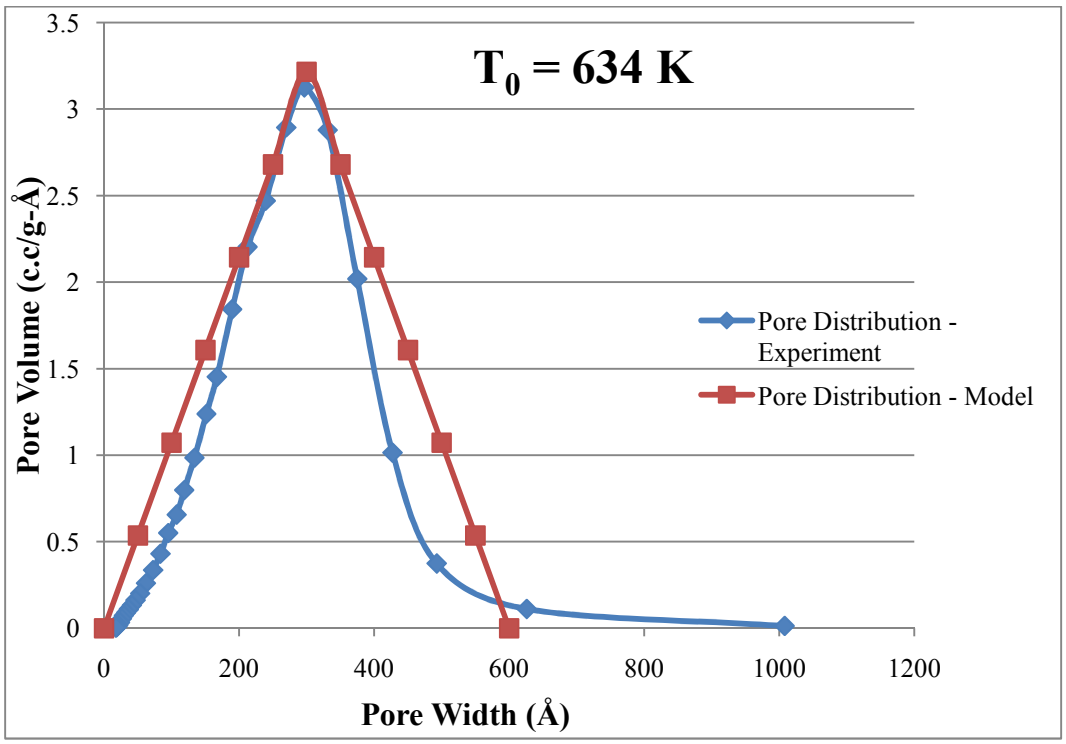
T0 = 634 K
Pore Volume (c.c/g-Å)
Pore Width (Å)
Pore Distribution - Experiment
Pore Distribution - Model
0
0.5
1
1.5
2
2.5
3
3.5
0
200
400
600
800
1000
1200

(c)

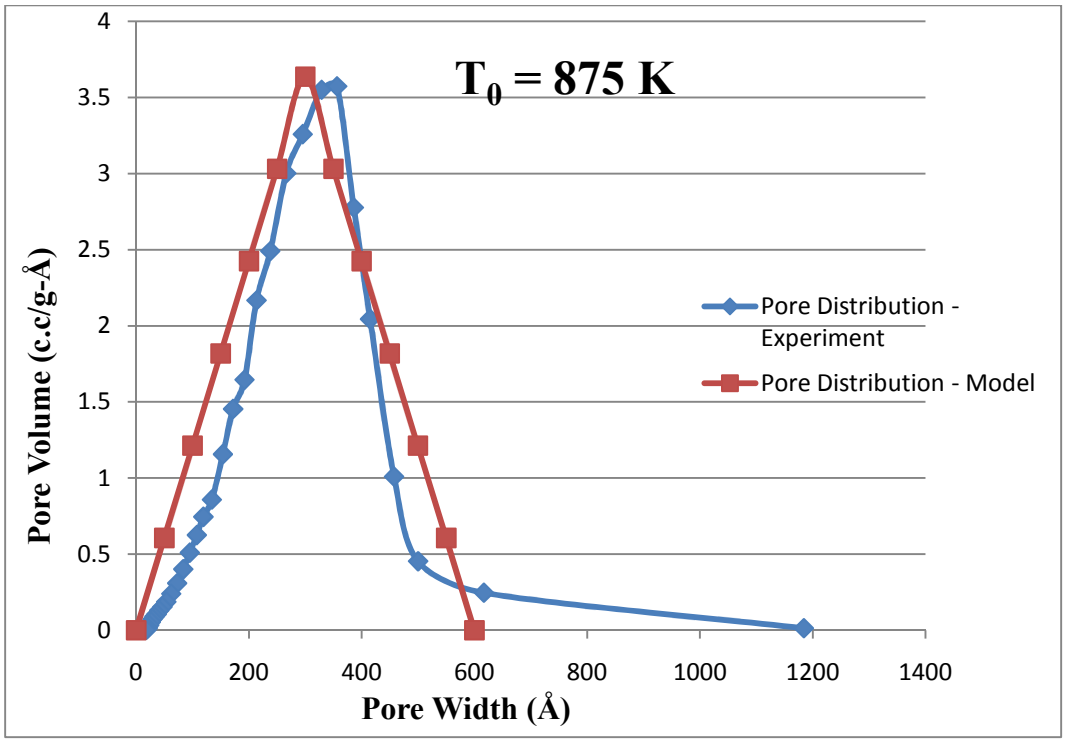

(d)

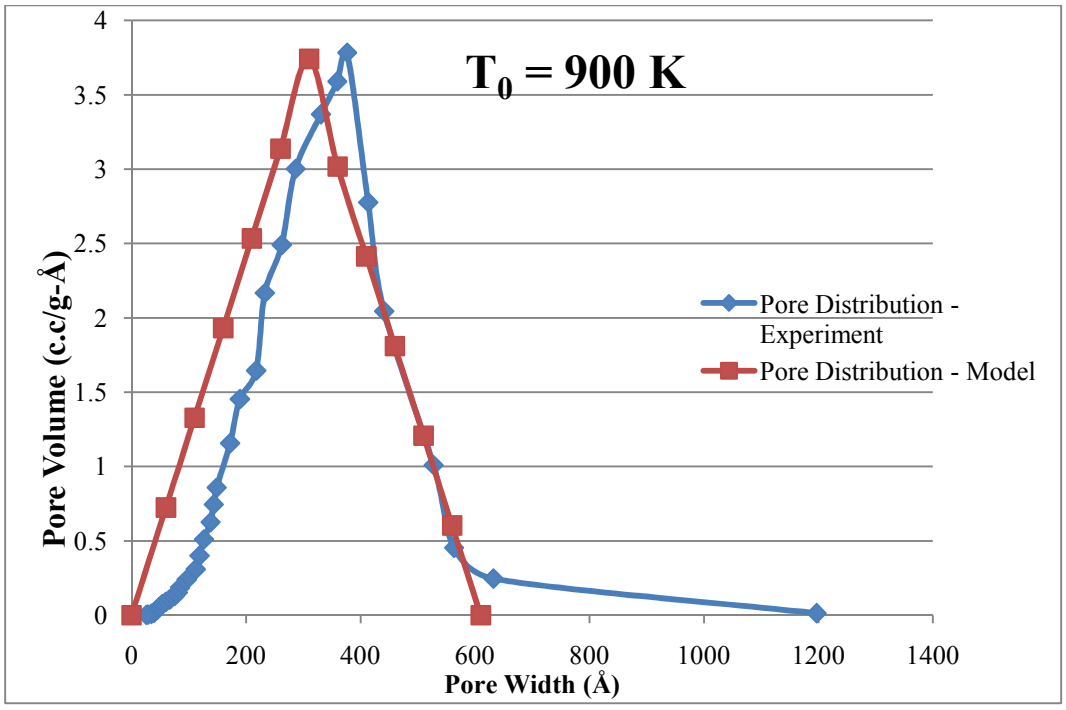

(e)

(a-e) Pore distribution comparison between experimental and math model

The above figures confirm the accuracy of the model in predicting the pore distribution based on the initial pre-heat temperature. The figure below shows the predicted pore distribution of processed gel from simulations.

Figure – 29

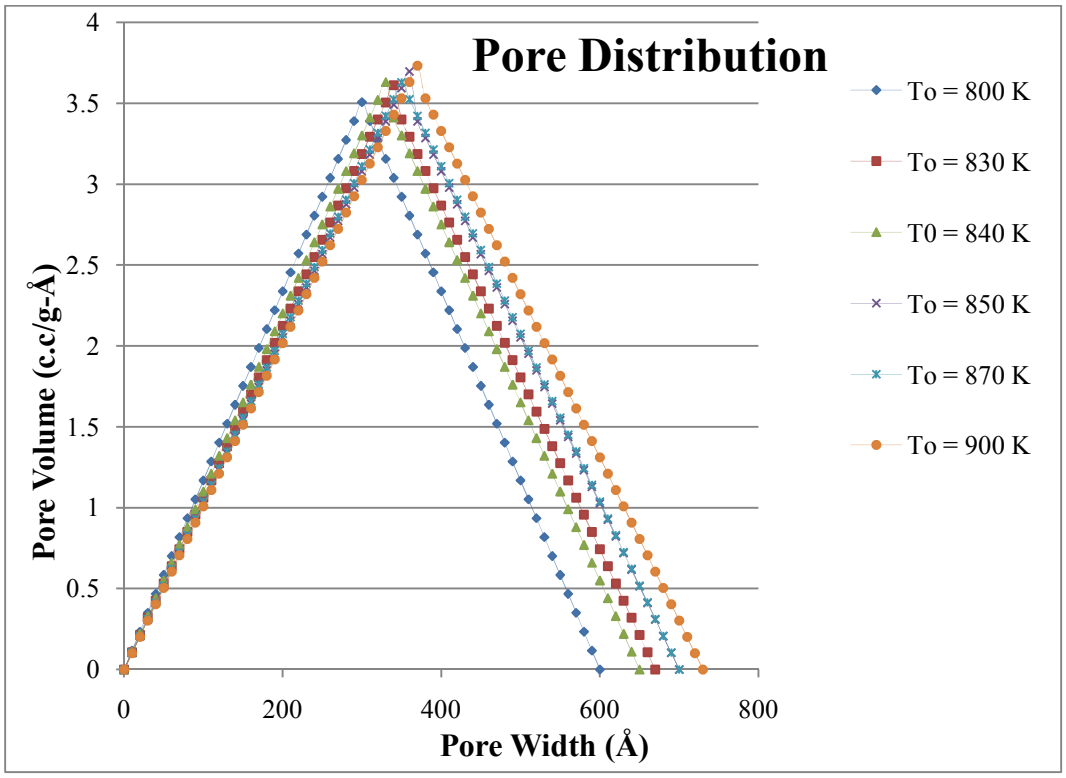

Predicted pore distribution from the mathematical model

The above figure shows the pore distribution of the processed gel from simulations based on the pre-heat temperature. The maximum pore volume is increasing and the curve is shifting towards increasing pore width as the pre-heat temperature increases. This is very similar to the pore distribution obtained from the experimental analysis.

4.3 Physical relation between average pore volume and initial temperature

Stephen Brunauer, P.H. Emmett and Edward Teller proposed a formula for a physical relation between average pore volume and temperature. The formula is slightly modified to fit my experimental process and is as follows

$$V_P = \frac{3}{4}\rho\frac{m_f}{w}\int_{T_o}^{T_\infty} L(T)dT$$

V_P = Pore volume (m^3/g-Å)

ρ = density of gel (kg/ m^3)

m_f= Mass fraction

w = width of the pore (Å)

L(T)dT = Length of the pore (Å)

T_0 = Initial pre-heat temperature (K)

T_∞= Steady state temperature (K)

L(T) is determined by a constant c, given by

$$c = \frac{-2\,m_f}{k\log_e\frac{T_o}{T_\infty}}$$

k = gas constant = 8.314 J/mole-K

Calculating the values of c using the data from the experimental process, the value of c lies between 0.129 and 2.233. According to data available from the paper written for BJH theory.

$$0.1 \le c \le 1 \quad L(T) = \alpha_o T$$

$$1 \le c \le 10 \quad L(T) = \alpha T + \beta$$

$\alpha_o = 1.2967 \times 10^{-5}$, $\alpha = 3 \times 10^{-4}$, $\beta = 0.3044$

The physical relation is used to obtain the average pore volume for the experimental process with initial temperature and mass fraction as variables.

Table – 13

S.No	Pre-heat temperature (K)	Mass fraction	Constant c	Average pore volume (cm^3/g-Å)
1	273	0.52	0.129	1.31
2	424	0.49	0.209	1.55
3	634	0.55	0.751	1.62
4	875	0.53	1.212	1.8
5	900	0.5	1.175	1.86
6	900	0.67	1.575	1.91
7	900	0.78	1.833	2
8	900	0.86	2.021	1.97
9	900	0.95	2.233	2.1

Average pore volume from physical relation

4.4 Pore distribution comparison between experimental analysis and physical model

The above table and the model discussed in section 4.2 can be used to obtain the pore distribution. A comparison between the results obtained from experimental analysis and physical model is shown in the following Figure – 30

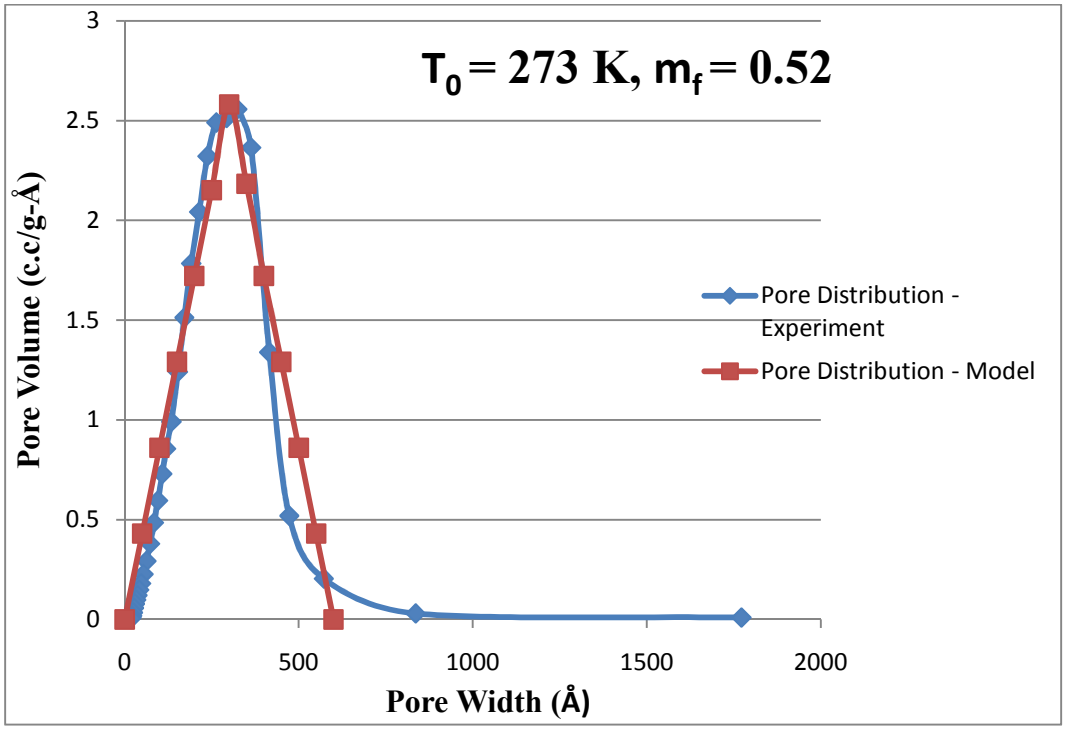

(a)

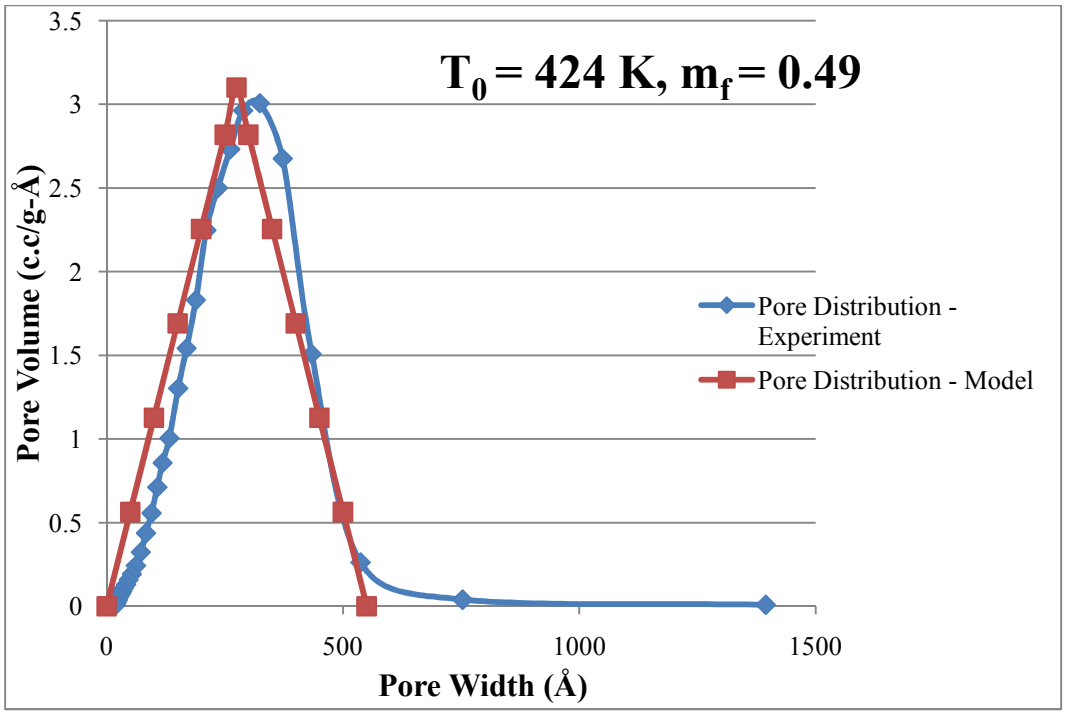
T_0 = 424 K, m_f = 0.49
Pore Volume (c.c/g-Å)
Pore Width (Å)
Pore Distribution - Experiment
Pore Distribution - Model
0
0.5
1
1.5
2
2.5
3
3.5
0
500
1000
1500

(b)

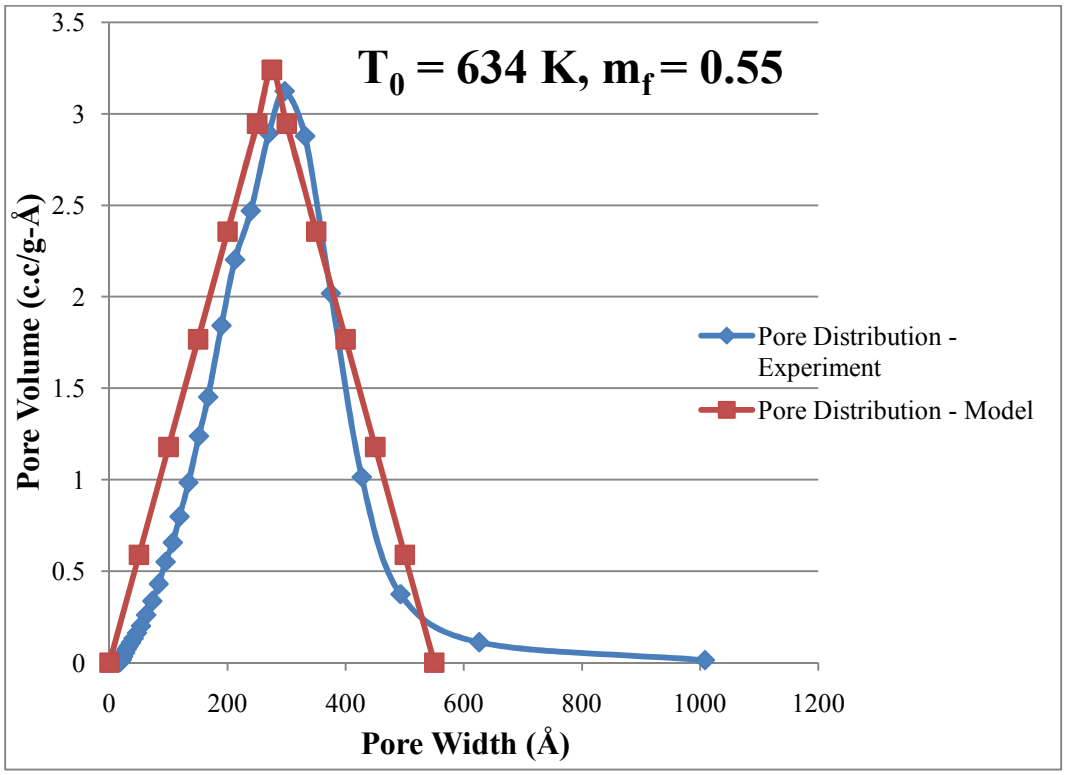
T_0 = 634 K, m_f = 0.55
Pore Volume (c.c/g-Å)
Pore Width (Å)
Pore Distribution - Experiment
Pore Distribution - Model
0
0.5
1
1.5
2
2.5
3
3.5
0
200
400
600
800
1000
1200

(c)

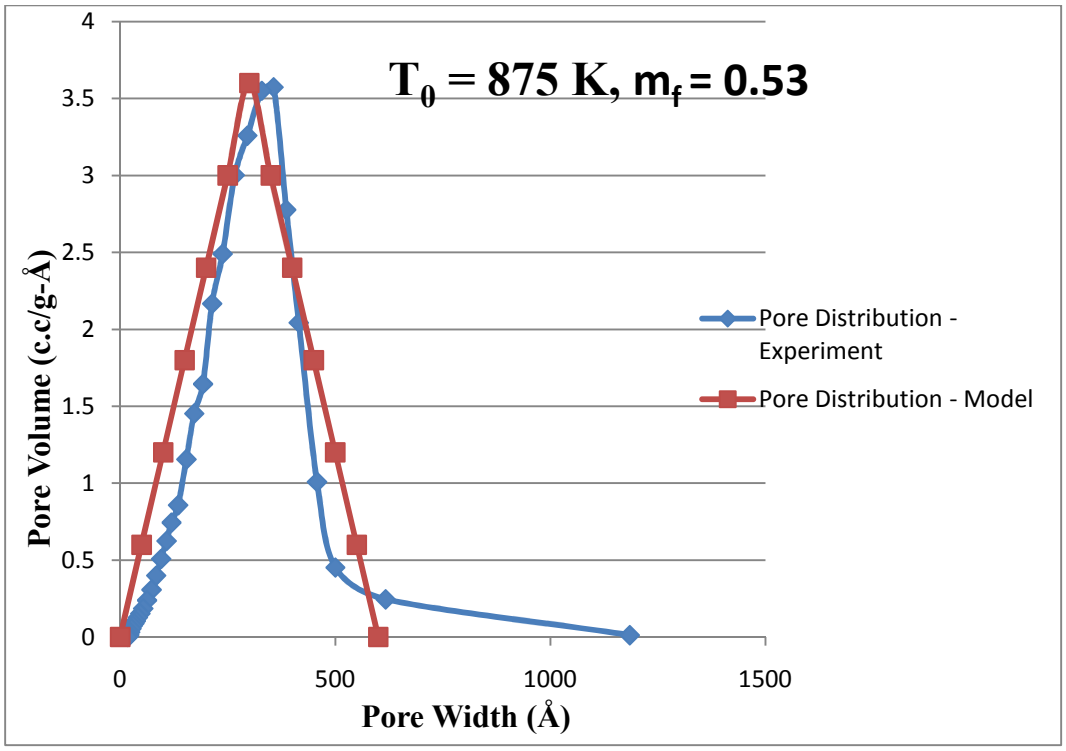
T_0 = 875 K, m_f = 0.53
Pore Volume (c.c/g-Å)
Pore Width (Å)
0
0.5
1
1.5
2
2.5
3
3.5
4
0
500
1000
1500
Pore Distribution - Experiment
Pore Distribution - Model

(d)

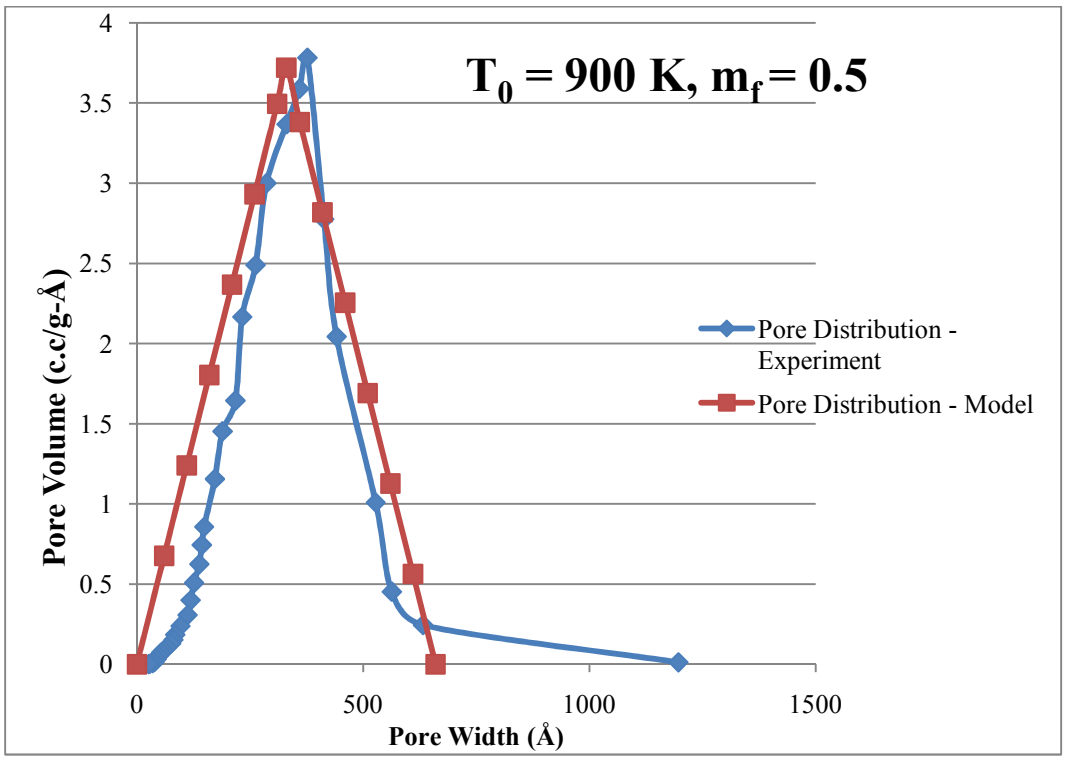
T_0 = 900 K, m_f = 0.5
Pore Volume (c.c/g-Å)
Pore Width (Å)
0
0.5
1
1.5
2
2.5
3
3.5
4
0
500
1000
1500
Pore Distribution - Experiment
Pore Distribution - Model

(e)

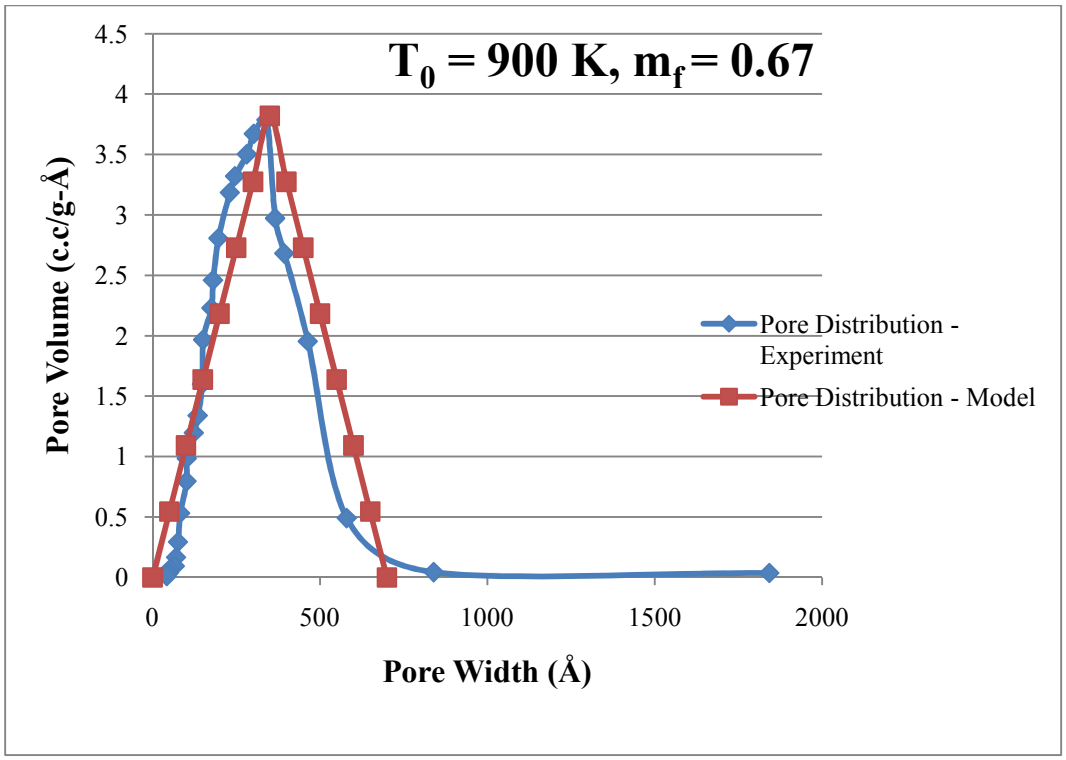
$T_0 = 900$ K, $m_f = 0.67$
Pore Volume (c.c/g-Å)
Pore Width (Å)
Pore Distribution - Experiment
Pore Distribution - Model
0
0.5
1
1.5
2
2.5
3
3.5
4
4.5
0
500
1000
1500
2000

(f)

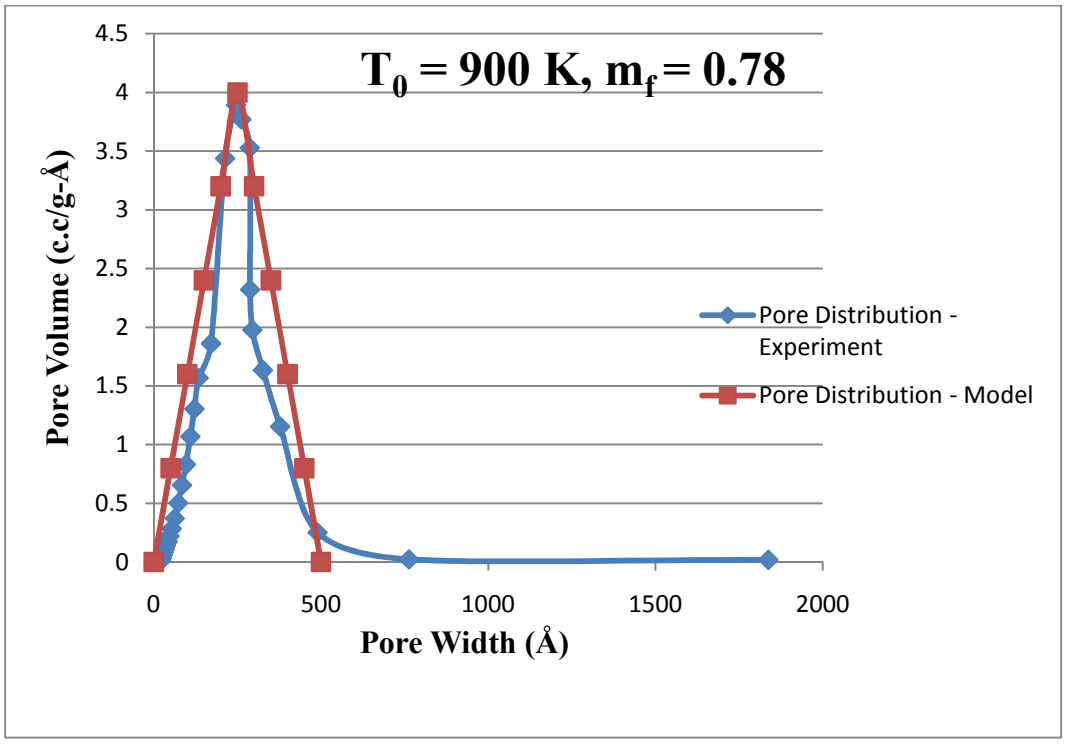
$T_0 = 900$ K, $m_f = 0.78$
Pore Volume (c.c/g-Å)
Pore Width (Å)
Pore Distribution - Experiment
Pore Distribution - Model
0
0.5
1
1.5
2
2.5
3
3.5
4
4.5
0
500
1000
1500
2000

(g)

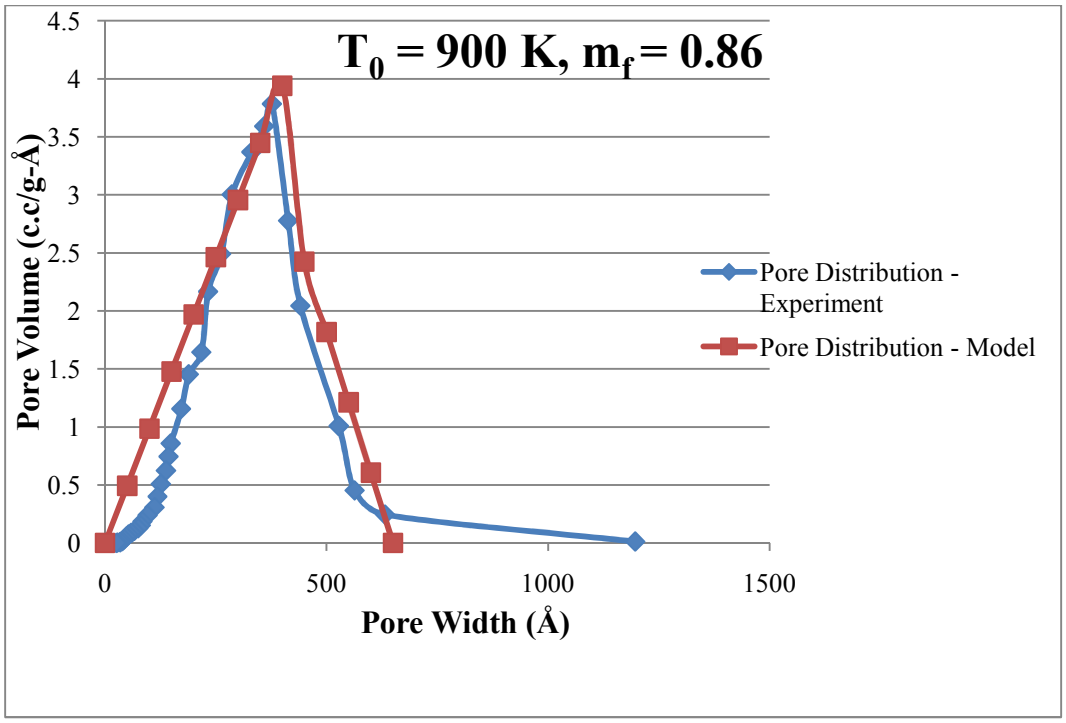

(h)

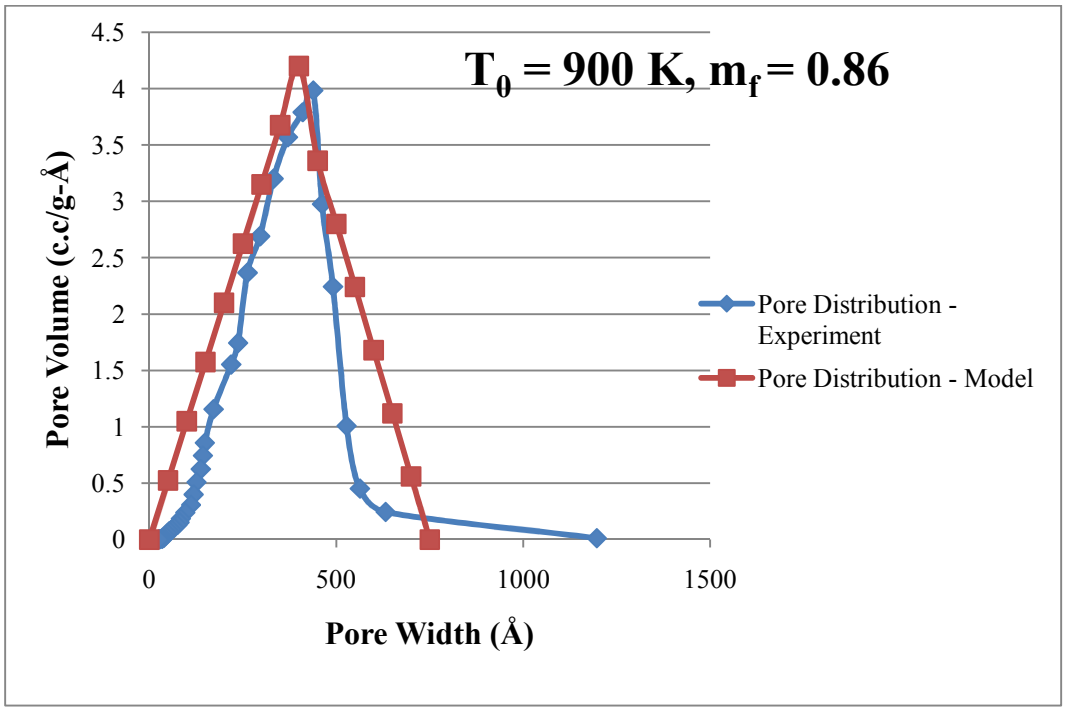

(i)

(a-i) Pore distribution comparison between experimental and physical model

Chapter 5

Conclusion and Recommendations

5.1 Conclusion:

This document discusses the preparation of pyro-gel used in the experimental analysis, its main constituents, behavior of pyro-gel when subject to heat and oxygen at various pre-heat conditions and previous similar research work done on different types of gels.

An experimental analysis of burning of pyro-gel is done using two types of reactor setups at various input conditions and the temperature distribution for both the setups is obtained. The residue obtained after the experimental procedure is analyzed and the pore distribution is obtained. A discussion is made on the temperature distribution and is it a true reflection on the desired behavior of the pyro-gel subject to heat and oxygen. The pore distribution of the fuel residues obtained at various pre-heat conditions is used to observe the effect initial temperature has on the burning of pyro-gels. An attempt is made to find the effect initial oxygen content available to the pyro-gel for burning has on the pore distribution.

Simulations are run using two models, non pre-mixed and pre-mixed porous model to try to emulate the experimental procedure involving the second reactor setup. Temperature distributions are obtained for both the models and comparison is done with the results obtained from the experimental analysis. A discussion is made on both the models and their accuracy in trying to replicate the experimental

procedure and if the temperature distributions obtained reflect the results obtained from the experimental analysis.

A mathematical and physical model to predict the pore distribution with initial pre-heat temperature and mass fraction of gel as functions is proposed based classic BET/BJH theories. The pore distribution obtained from the mathematical and physical model is compared to that obtained from the experimental analysis to validate the accuracy of the model.

5.2 Recommendations:

The experimental setup used for the analysis was very basic with two thermocouples and a heat source along with the reactor for pyro-gel burning. The setup can be much more elaborate and use more than two thermocouples to obtain temperatures at various points, pressure sensors to obtain pressure, gas sensors to obtain concentration oxygen at various stages of the experimental procedure.

The chemical equation used for the simulation model is obtained from another experimental process under similar conditions. Few assumptions were incorporated into the model when using the particular equation. An extensive chemical kinetic analysis would help in obtaining a much better equation with the required constants and will the make the model much more accurate.

REFERENCES

[1] Emel I. Goksu , Matthew I. Hoopes , Barbara A. Nellis , Chenyue Xing , Roland Faller, Curtis W. Frank , Subhash H. Risbud, Joe H. Satcher Jr. and Marjorie L. Longo, Silica xerogel/aerogel-supported lipid bilayers: Consequences of surface corrugation. Biochemica et Biophysica Acta, 2010; 1798: 719-729.

[2] Alexander E. Gash, Joe H. Satcher Jr., and Randall L. Simpson, Strong Akaganeite Aerogel Monoliths Using Epoxides: Synthesis and Characterization. Chem. Mater. 2003; 15: 3268-3275

[3] Elliot P. Barrett, Leslie G. Joyner and Paul P. Halenda, Determination of Pore Volume and Area Distributions in Porous Substances. J. Am. Chem. Soc. 1951; 73 (1): 373–380

[4] Maria I.F. Macedo, Carla C. Osawa and Celso A. Bertran, Sol-Gel Synthesis of Transparent Alumina Gel and Pure Gamma Alumina by Urea Hydrolysis of Aluminum Nitrate. Journal of Sol-Gel Science and Technology. 2004; 30: 135–140.

[5] Theodore F. Baumann, Marcus A. Worsley, T. Yong-Jin Han and Joe H. Satcher Jr., High surface area carbon aerogel monoliths with hierarchical porosity. Journal of Non-Crystalline Solids. 2008; 354: 3513–3515.

[6] Ruowen Fu, Bo Zheng, Jie Liu, Steve Weiss, Jackie Y. Ying, Mildred S. Dresselhaus, Gene Dresselhaus, Joe Satcher, Jr. and Theodore Baumann, Studies of the Chemical and Pore Structures of the Carbon Aerogels Synthesized by Gelation and Supercritical Drying in Isopropanol. Journal of Applied Polymer Science. 2004; 91(5): 3060-3067

[7] Minh Tuan Nguyen, Tae-Jin Park and Dong Jin Suh, Synthesis of high-surface-area alumina aerogels by non-alkoxide sol-gel process. Theories and Applications of Chem. Eng. 2002; 8(2): 5298-5301.

[8] G. Urretavizcaya, A. L. Cavalieri, J. M. Porto Lopez, I. Sobrados, and J. Sanz, Thermal Evolution of Alumina Prepared by the Sol-Gel Technique. Journal of Materials Synthesis and Processing. 1998; 6(1): 1-7.

[9] Chang-Yeoul Kim, Jong-Kyu Lee and Byung-Ik Kim, Synthesis and pore analysis of aerogel–glass fiber composites by ambient drying method. Colloids and Surfaces A: Physicochem. Eng. Aspects. 2008; 313: 179–182.

[10] Shani Keysar, Gennady E. Shter, Yoram de Hazan, Yachin Cohen, and Gideon S. Grader, Heat Treatment of Alumina Aerogels. Chem. Mater. 1997; 9 (11): 2464-2467.

[11] Marcel Nguefack, Aurelian Florin Popa, Sylvie Rossignol and Charles Kappenstein, Preparation of alumina through a sol–gel process. Synthesis, characterization, thermal evolution and model of intermediate boehmite. Phys. Chem. Chem. Phys. 2003; 5: 4279–4289.

[12] Theodore F. Baumann, Alexander E. Gash, Sarah C. Chinn, April M. Sawvel, Robert S. Maxwell, and Joe H. Satcher, Jr., Synthesis of High-Surface-Area Alumina Aerogels without the Use of Alkoxide Precursors. Chem. Mater. 2005; 17: 395-401.

[13] Brady J. Clapsaddle, David W. Sprehn, Alexander E. Gash, Joe H. Satcher Jr. and Randall L. Simpson, A versatile sol–gel synthesis route to metal–silicon mixed oxide nanocomposites that contain metal oxides as the major phase. Journal of Non-Crystalline Solids. 2004; 350: 173–181.

[14] Alexander E. Gash, Thomas L. Tillotson, Joe J. Satcher Jr., Lawrence W. Hrubesh, Randall L. Simpson, New sol-gel synthetic route to transition and main-group metal oxide aerogels using inorganic salt precursors. Journal of Non-Crystalline Solids. 2001; 285: 22-28.

[15] James E. House, Principles of Chemical Kinetics. Kinetics of Reactions in Solid State, 229-262.

[16] Sumio Sakka and Hiromitsu Kozuka, Sol–Gel Science and Technology: Processing, Characterization and Applications. Aerogel Processing, 599-617.

[17] Jeffrey C. Brinker, George W. Scherer, The physics and chemistry of sol-gel processing. Drying, 453-509.

[18] S. O. Kucheyev, T. F. Baumann, C. A. Cox, Y. M. Wang, J. E. Bradby and A. V. Hamza, Chemical Kinetics of Tri-glyceride acids. International Journal of Chemical Kinetics. 2009; 12: 345-352.

[19] Albert D.F., Andrew G.R., Mendenhall R.S., Bruno J.W. Supercritical methanol drying as a convenient route to phenolic-furfural aerogels. J. Non-Cryst. Solids. 2001; 296: 1–9

[20] Biesmans G., Randall D., Français E., Perrut M., Polyurethane-based organic aerogels' thermal performance. J. Non-Cryst. Solids. 1998; 225: 36–40.